Catalytic reactors for highly exothermic reactions: Steady-state stability enhancement by magnetic induction

Axel Fache, Frederic Marias, Bruno Chaudret

Catalytic reactors for highly exothermic reactions: steady-state stability enhancement by magnetic induction

Dr. Axel Fache, Laboratoire de Thermique Energétique et Procédés – IPRA EA1932, Universite de Pau et des Pays de l'Adour/E2S UPPA, 64000 Pau, France

Pr. Frédéric Marias, Laboratoire de Thermique Energétique et Procédés – IPRA EA1932, Universite de Pau et des Pays de l'Adour/E2S UPPA, 64000 Pau, France

Pr. Bruno Chaudret, Laboratoire de Physique et Chimie des Nano-Objets – UMR 5215, Institut National des Sciences Appliquées de Toulouse / CNRS, 31077 Toulouse, France

Corresponding Author: Axel Fache a.fache@univ-pau.fr

Abstract

The thermal management of catalytic reactors dedicated to highly exothermic reactions is often challenging, due to the existence of a positive thermal feedback. Up to now, many design and control options have been used to operate such reactors safely and efficiently. The present study examines the theoretical benefit of resorting to an alternative stabilization strategy based on the use of induction-heated pellets. Under given inductive conditions, the thermal power released by these pellets is a decreasing function of their temperature (negative thermal feedback). Wall-cooled fixed-bed methanation reactors containing mixed catalytic and induction-sensitive pellets are simulated numerically. The steady-state behavior of reactors enhanced by induction is compared to the behavior of conventional reactors. It is shown that the parametric sensitivity of induction reactors is lower than that of a conventional reactor achieving the same conversion. Induction reactors also demonstrate an ability to reach a higher chemical yield than a conventional reactor, before entering the runaway region. The impact of the operation conditions (inductive field, coolant temperature) and of the induction-sensitive pellets properties (absorption rate as a function of temperature) on the stabilization is analyzed.

keywords: exothermic reaction, methanation, fixed-bed reactor, numerical simulation, magnetic induction, stability

Notations

$a_{v\,cat}$	External surface area of catalyst pellets per unit of apparent volume, m^{-1}
$a_{v\,inert}$	External surface area of inert pellets per unit of apparent volume, m^{-1}
B_0	Porous medium permeability, m^2
C_{cat}	Catalytic solid heat capacity, J/K/kg
C_i	Molar concentration of species i in the gas mixture, mol/m^3
C_{inert}	Inert solid heat capacity, J/K/kg
$C_{p\,gas}$	Isobaric heat capacity of the gas mixture, J/K/kg
C_{p_i}	Isobaric heat capacity of species i, J/K/kg
C_{tot}	Total molar concentration of gaseous species, mol/m^3_{gas}
C_{v_i}	Isochoric heat capacity of species i, J/K/kg
$D_{e,ij}$	Effective binary diffusion coefficient of i in j, m^2/s
$D_{er,i}$	Effective radial dispersion coefficient i, m^2/s
$D_{Kn,i}$	Knudsen diffusion coefficient of species i, m^2/s
$D_{m,i}$	Molecular diffusion coefficient of i, m^2/s
$D_{m,\ ij}$	Binary diffusion coefficient of i in j, m^2/s
d_p	Pellets diameter, m
e_{tube}	Tube wall thickness, m
f_{cat}	Proportion of catalytic pellets, in the pellets mixture
f_{inert}	Proportion of inert pellets, in the pellets mixture
h_{c-t}	Equivalent coolant to tube heat transfer coefficient (actually accounting for tube wall resistance), $W/K/m^2_{c\text{-}t}$
h_i	Specific enthalpy of gas species i, J/K/kg
h_{s-g}	Solid-gas heat exchange coefficient, $W/m^2/K$
J_i	Flux of species i at pellet scale, $mol/s/m^2_{tot}$
K_{valve}	Valve characteristic coefficient, $m^3.s/Pa$
L	Total tube length, m
L_{reac}	Length of the reaction zone, m
M_i	Molecular weight of gaseous species i, kg/mol
$\mathcal{P}$	Specific absorption rate (thermal power due to induction), W/kg_{inert}
P	Total pressure, Pa

P_i	Partial pressure of species i, Pa
P_{out}	Post-outlet valve pressure, Pa
$\mathcal{P}_T$	Ideal slope of the specific absorption rate as a function of temperature, W/K_{inert}/kg_{inert}
$\dot{Q}_{chem}$	Power released by the reaction, W
$\dot{Q}_{exch}$	Thermal power withdrawn from the reaction medium, W
$\dot{Q}_{gen}$	Thermal power generated in the reaction medium, W
$\dot{Q}_{induc}$	Thermal power due to the induction, W
Q_{inj}	Molar flow rate of injected gas mixture, mol/s
$Q_{inj,i}$	Molar flow rate of injected species i, mol/s
Q_i^{out}	Molar outflow rate of species i, mol/s
R	Ideal gas constant, 8.314 J/mol/K
r	Radial location in cylindrical coordinates (macroscopic scale), m
Re_0	Superficial Reynolds number, -
$\dot{r}_i^m$	Specific formation rate of species i, mol/s/kg_{cat}
R_i^v	Formation rate of species i per apparent volume, mol/s/m^3_{total}
r_{pore}	Micropore radius, m
R_{reac}	Internal radius of the tube = radius of the reaction medium, m
R_{tube}	Outer diameter of the tube, m
S	Surface area (generic), m²
S_{reac}	Internal cross-section of the tube, m²
S_{tube}	Cross-section of the tube wall, m²
$s_{\phi\backslash X}, S_{\phi\backslash X}$	Absolute and normalized sensitivities of quantity ϕ to parameter X
t	Time, s
T	Temperature, K (generic notation)
T_{cat}	Catalyst temperature, K
T_{cool}	Coolant temperature, K
T_{extr}	Extrapolation temperature as defined on figure 3, K
T_{gas}	Temperature of the macroscopic gas, K
T_{gas}^{inj}	Inlet gas temperature, K
T_{inert}	Inert solid temperature, K

T_{tube}	Tube wall temperature, K
u_i	Specific internal energy of gas species i, J/K/kg
v_z	Axial superficial velocity, m/s
Y_{CH4}	Methane yield, -
z	axial location, m
Greek letters	
δX	Increment of quantity X
$\Delta_r H^0$	Standard enthalpy of reaction, J/mol
ϵ	Macroscopic void fraction, -
ϵ_{mic}	Microscopic void fraction (inside catalytic pellets), -
ϵ_{ni}	Non-ideality parameter as introduced on figure 3 and equation 12, -
ι	Relative instability as defined in equation 1, -
λ_{cat}	Thermal conductivity of the catalytic pellet, W/m/K
$\lambda^{cat-cat}$	Effective conductivity for catalyst-catalyst thermal transfer, W/m/K
$\lambda^{cat-inert}$	Effective conductivity for catalyst-inert thermal transfer, W/m/K
λ_{er}^{gaz}	Effective radial conductivity of the gas mixture, W/m/K
λ_{gas}	Thermal conductivity of the gas mixture, W/m/K
λ_i	Thermal conductivity of species i, W/m/K
λ_{inert}	Thermal conductivity of the inert pellet, W/m/K
$\lambda^{inert-inert}$	Effective conductivity for inert-inert thermal transfer, W/m/K
λ_{tube}	Thermal conductivity of the tube wall, W/m/K
μ_{eff}	Effective viscosity, Pa.s
μ_{gas}	Dynamic viscosity of the gas mixture, Pa.s
μ_i	Viscosity of pure species i, Pa.s
$\mu_{i,mix}$	Viscosity of species i in the gas mixture, Pa.s
ξ	Radial location in spherical coordinates (pellet scale), m
ρ_{cat}	Mass of catalytic pellets per unit of total volume, in the absence of inert pellets, kg/m^3
ρ_{cat}^{mic}	Mass of a catalytic pellet per unit of pellet volume, kg/m^3
ρ_{cat}^{mix}	Mass of catalytic pellets per unit of apparent volume, kg/m^3
ρ_{gas}	Gas mixture density, kg/m^3

ρ_{inert}	Mass of inert pellets per unit of total volume, in the absence of catalytic pellets, kg/m^3
ρ_{inert}^{mic}	Mass of a inert pellet per unit of pellet volume, kg/m^3
ρ_{inert}^{mix}	Mass of inert pellets per unit of apparent volume, kg/m^3
$(\rho C)_{tube}$	Volumetric heat capacity of the tube wall, J/K/m^3
τ	Tortuosity, -
ϕ	Heat flux, W/m²
ϕ_{c-t}	Heat flux from the coolant to the tube, W/m²
ϕ_{cat-g}	Heat flux from catalytic solid to macroscopic gas, W/m²
$\phi_{inert-g}$	Heat flux from inert solid to macroscopic gas, W/m²
ϕ_{t-cat}	Thermal flux from tube wall to catalyst, W/m²
ϕ_{t-g}	Thermal flux from tube wall to macroscopic gas, W/m²
ϕ_{t-gs}	Thermal flux from tube wall to macroscopic gas and solids, W/m²
$\phi_{t-inert}$	Thermal flux from tube wall to inert solid, W/m²
χ_i	Molar fraction of species i in the gas mixture, -
Subscripts	
0	Under standard conditions
cat	For catalytic pellets
$cool$	For the coolant
$c-t$	Associated with the coolant-tube wall interface
gas	For the gas mixture
i	For gas species i
$inert$	For inert pellets
mic	At microscopic (sub-pellet) scale
Superscripts	
$dwstr$	At downstream non-porous zone conditions
mix	In a mixture of two kinds of pellets
$pert$	After perturbation
$upstr$	At upstream non-porous zone conditions
∞	In infinite medium (far from any wall)

1. Introduction

1.1. Thermal stability : theory and existing technologies

Cooled reactors are commonly used to complete highly exothermic heterogeneous catalytic reactions (e.g. hydrogenation or oxidation of organic compounds). Due to the mixed effects of the temperature on the reaction, the design and control of such reactors are subject to thermal management difficulties. Too low a temperature implies that the reaction rate is insufficient, while a temperature excess can damage the catalyst and be detrimental to the conversion of the reactants (thermodynamic limitations). As long as the thermodynamic equilibrium is not reached, a positive feedback takes place between the temperature of the reaction medium, the reaction rate and the thermal power released by the reaction. It comes as a consequence that high parametric sensitivity and thermal runaway can be encountered [1, 2].

Since the vocabulary can differ from an author and a framework to another, the definitions used in the present paper need a clarification before going any further:

- "parametric sensitivity" quantifies the steady-state difference of a quantity of interest (e.g. reaction medium temperature) subsequent to the perturbation of a design or operation parameter.
- "thermal runaway" refers to a self-increasing temperature after a perturbation (dynamic concept).
- in a "stable" operation region, parametric sensitivity remains moderate. Crossing the limit of a stable region typically triggers a runaway, which leads to a new steady-state temperature that is much higher than the pre-runaway temperature (high parametric sensitivity).

Using these definitions, the effect of the (de)stabilizing phenomena can be approached via the theory of thermal explosion [3, 4]. In the simplest case, the reaction medium is considered invariant in space (0-D representation) and the temperature of all the phases is equal to T. After a temperature increase δT, the thermal power that is generated in the reaction medium increases by $\delta \dot{Q}_{gen}$ and the thermal power that is withdrawn from the reaction medium increases by $\delta \dot{Q}_{exch}$. One can then define the relative instability ι according to equation 1.

$$\iota = \frac{\delta \dot{Q}_{gen}/\delta T}{\delta \dot{Q}_{exch}/\delta T} \quad \text{(Eq. 1)}$$

A strong positive feedback in the reaction medium (numerator) tends to increase the parametric sensitivity and shrink the stable region. A reactor avoids a runaway if the stabilizing effects are stronger than the destabilizing ones, which requires that $\iota < 1$. When the reaction medium can't be considered zero-dimensional (e.g. for tubular fixed-bed reactors), this qualitative reasoning remains valid although the above-mentioned criterion needs an adaptation to remain relevant (e.g. applying it locally to special points [1, 5]).

From a technological point of view, the goal of keeping ι sufficiently low can be achieved thanks to various strategies. First, it should be noticed that industrial systems are often made-up of two (or more) reactors in series. The upstream reactor is mainly driven by kinetics, whereas the downstream reactor is meant to reach the highest possible chemical yield (thermodynamic equilibrium) [6, 7]. The destabilizing effects are thereby mainly concentrated on the kinetic-driven reactor.

If the reactor is operated with a constant coolant temperature, the denominator of ι can be increased via the enhancement of the thermal transfer from the reaction medium to the coolant. Fluidized-bed reactors are effective on this point, but the associated backmixing is disadvantageous in terms of chemical efficiency. On the opposite, fixed-bed reactors don't suffer significantly from backmixing effects but the thermal transfer tends to be lower. This observation led to the development of intensified reactors [8], which are basically equivalent to numerous reaction channels in parallel: the smaller the hydraulic diameter of the channel, the better the heat exchange. These devices can be very compact, however they are prone to premature fouling and imply high manufacturing cost.

Rather than increasing the denominator of ι, one can moderate the heat production rate variations (numerator). Catalytic pellets with very small pore radius can provide this moderation (diffusional limitations). Alternatively, one can mix the catalytic pellets with inert pellets. The inert pellets can be chosen so they have a high thermal conductivity, which as a side-effect enhances the denominator. Of course this design method tends to increase the bulkiness of the reactor, although the proportion

of inert pellets can be non-uniform for a better use of the reaction volume [5, 9]. In any case, the moderation of the numerator has to be a compromise between efficiency and safety.

Further improvement can be obtained if the coolant temperature is a function of the conversion instead of being constant. As underlined by Bremer et al. [10] after Eigenberger & Schuler [11], the operation of a system can be safe even if the reactor itself is in an unstable region, provided that adjustments can be applied with a characteristic time shorter than that of the divergent phenomena. Equation 1 includes the signature of such a control. Indeed, $\dot{Q}_{gen}$ is directly related to the conversion of the reactants (enthalpy of reaction and reaction rate). When the coolant temperature is a function of the conversion, so is $\dot{Q}_{exch}$. In the end, a proper control implies that $\dot{Q}_{exch}$ varies faster than $\dot{Q}_{gen}$ so that ι remains low enough for the {reactor + control} system.

To conclude this paragraph, one can underline that whether operation in a stable or in an unstable region of the reactor is chosen, the existence of stabilizing effects is beneficial. If operation in a stable region is preferred, stronger negative feedbacks provide the advantage of extending said region. If operation in an unstable region is chosen, the negative feedbacks can moderate the divergent evolution of the system over time, thus providing more leeway and facilitating the adjustments of the coolant temperature (better stability of the {reactor + control} system).

1.2. Magnetic induction as a temperature stabilizer

Induction-sensitive pellets can be included in the medium constituting the active zone of a thermo-chemical component, making it possible to provide heat to the immediate vicinity of the particles/fluids that need to be heated-up. Many thermo-chemical processes can potentially be enhanced by this technology (e.g. drying or endothermic reactions [12-14]). The induction sensitive pellets can be made of a conventional conductive material, but it can also contain specific nanomaterials. The heating properties of nanoparticles subject to an inductive magnetic field (e.g. Curie temperature) depend on both their chemical composition and their geometrical properties (size and shape) [15-17]. This constitutes an advantage of nanoparticles, since each material can lead

to a variety of heating properties that would not be accessible if the same material was used under a conventional form. Moreover some nanoparticles can absorb magnetic energy (and turn it into heat) more efficiently than conventional materials: the required magnetic field amplitude is lower with such nanomaterials, which makes it more suitable to industrial-scale components [18].

While induction heating provides a straightforward advantage for endothermic reactions, it seems counterproductive for highly exothermic reactions. Applying inductive heating to the reaction medium requires an overcooling of the reactor in order to keep the energy terms balanced (figure 1). This is of course unfavorable as regards the energy efficiency, however it is expected to provide a two-fold advantage in terms of stability.

i) First, under given inductive conditions, the specific absorption rate of the induction-sensitive pellets decreases when temperature increases [15, 19]. This constitutes an intrinsic negative feedback. More precisely, the thermal power generation $\dot{Q}_{gen}$ can be broken-down into two sub-terms:

   $\dot{Q}_{gen} = \dot{Q}_{chem} + \dot{Q}_{induc}$ (Eq. 2)

   where $\dot{Q}_{chem}$ is the power released by the reaction, and $\dot{Q}_{induc}$ is the thermal power due to the induction. Equation 1 becomes

   $\iota = \frac{\delta\dot{Q}_{chem}/\delta T + \delta\dot{Q}_{induc}/\delta T}{\delta\dot{Q}_{exch}/\delta T}$ (Eq. 3)

   with $\delta\dot{Q}_{induc}/\delta T \leq 0$ (stabilizing effect of induction).

ii) Second, the inductive field itself can be controlled with a very short characteristic time: the combination of overcooling and instant induction control can be deemed equivalent to controlling the heat withdrawal instantly. This strategy is particularly interesting to operate in unstable regions of the reactor (quick adjustments).

The present work focuses on the effect of the intrinsic negative feedback under constant inductive field conditions, at steady state (expected advantage #i). The methanation of CO_2 is considered as the case study:

$$CO_2 + 4 \cdot H_2 \rightleftharpoons CH_4 + 2 \cdot H_2O,\ \Delta_r H^0 = -165\ kJ \cdot mol_{CO2}^{-1}$$

with side reactions:

$$CO_2 + H_2 \rightleftharpoons CO + H_2O,\ \Delta_r H^0 = 41\ kJ \cdot mol_{CO2}^{-1}$$

$$CO + 3 \cdot H_2 \rightleftharpoons CH_4 + H_2O,\ \Delta_r H^0 = -206\ kJ \cdot mol_{CO}^{-1}$$

This set of reactions has been subject to growing research interest in recent years, due to its potential application to energy transition (power-to-gas, upgrading of product gas from waste and biomass valorization processes) [7, 20, 21].

A mathematical model predicting the behavior of a wall-cooled fixed-bed reactor with optional induction heating is described. Simulations are performed so that an induction reactor is compared to a conventional one, in terms of parametric sensitivity. The effects of the overcooling temperature and of the induction-sensitive pellets properties on the parametric sensitivity are examined. It is then shown that an induction reactor can avoid a runaway under conditions that are compatible with a higher methane yield than a conventional reactor (stable region extension).

2. Method

2.1. Mathematical model

2.1.1. Model overview

This paragraph reports the key points of the mathematical model that is used in the sequel. More details on the model assumptions, justification and development can be found in previous work by Fache & Marias [22]. The modeled reactor is shown on figure 2. A multi-scale representation is chosen for mass and momentum balances (2-D at macroscopic scale, 1-D at intraparticular scale). The macroscopic concentration of gaseous species i is a function of the two macroscopic coordinates $\left(C_i(r,z)\right)$ whereas the microscopic concentration is a function of 3 coordinates $\left(C_i(\xi,r,z)\right)$. The temperatures are functions of the macroscopic coordinates (r,z) only: the intraparticular temperature gradients are ignored, and the microscopic gas is in thermal equilibrium with the surrounding solid. Three temperatures are distinguished: macroscopic gas phase (T_{gas}), catalytic

microporous solid (T_{cat}), and inert solid pellets (T_{inert}).The pellets are assumed to be perfectly mixed (no segregation), so the two solids are entangled. The inert pellets can be heated by induction.
The main balance equations constituting the model are reported tables 1 and 2. It should be noticed that even though the present study addresses steady-state issues only, the developed model is fully dynamic.

2.1.2. Absorption rate – control and temperature dependence

Since the aim of the present study is to examine the stabilizing effect of inductive heating, the specific absorption rate $\mathcal{P}$ in equation 10 deserves extra attention:

- $\mathcal{P}$ is proportional to the hysteresis heating per loop cycle (J/kg). This heating depends on the properties of the nanoparticles, the applied magnetic field amplitude, and the temperature of the nanoparticles. The latter aspect is of special interest for the present work.
- For a given heating per loop cycle, $\mathcal{P}$ can be controlled through the frequency of the magnetic field. Also, for a given set {field amplitude, field frequency}, the magnetic field can be pulsed (with adjustable periods between successive pulses). The characteristic time of said pulses is far shorter than the typical characteristic times of thermal inertia, so that $\mathcal{P}$ can be deemed continuous (in the mathematical sense of the term) in a context of process engineering.

Vinum et al. [14] established the temperature dependence of the heating loop in the case of CoNi nanoparticles. As illustrated figure 3, $\mathcal{P}\ (T)$ decreases with a variable slope until it gradually cancels around the Curie temperature. One can notice that there is a significant range of temperatures where $\mathcal{P}\ (T)$ is relatively linear, starting about 300 K and ending about 100 K below the Curie temperature. The intersection of the linear approximation with the horizontal axis enables to introduce the extrapolation temperature T_{extr} (about 50 K below Curie temperature); the inductive power at this temperature is only a small fraction ϵ_{ni} of the power obtained at low temperature. Assuming the $\mathcal{P}\ (T)$ curve has the same shape for the nanoparticles that would be of interest for the present reaction (except their Curie temperature would be different from that of Vinum et al.'s particles), two $\mathcal{P}\ (T)$ models are considered in the present study (figure 4).

The idealized model reads:

$\mathcal{P}(r,z) = \mathcal{P}_T \cdot \left(T_{extr} - T_{inert}(r,z)\right)$ if $T_{extr} - 200\ K < T_{inert}(r,z) < T_{extr}$;

$\mathcal{P}(r,z) = 0$ if $T_{inert}(r,z) \geq T_{extr}$ (Eq. 11)

The non-idealized model takes into account the fact that $\mathcal{P}$ cancels very gradually at high temperature, in a conservative manner:

$$\mathcal{P}(r,z) = \mathcal{P}_T \cdot \left[\left(T_{extr} - T_{inert}(r,z)\right) + \epsilon_{ni} \cdot (T_{extr} - T_0) \cdot \exp\left(-15 \cdot \frac{T_{extr} - T_{inert}(r,z)}{T_{extr} - T_0}\right)\right]$$

if $T_{extr} - 200\ K < T_{inert}(r,z) < T_{extr}$;

$$\mathcal{P}(r,z) = \mathcal{P}_T \cdot (T_{extr} - T_0) \cdot \epsilon_{ni} \cdot \exp\left(\left(\frac{1}{\epsilon_{ni}} - 15\right) \cdot \frac{T_{extr} - T_{inert}(r,z)}{T_{extr} - T_0}\right)$$ if $T_{inert}(r,z) \geq T_{extr}$ (Eq. 12)

Where $\mathcal{P}_T$ is the ideal slope of the function $\mathcal{P}(T)$, for the considered nanoparticles and operation conditions. The operation conditions (magnetic field amplitude & frequency, or duration of the pulses) are not explicitly visible in the model. Rather, their values are implicitly expressed via the value of $\mathcal{P}_T$.

T_0 is a reference temperature, that is set at 273.15 K. $\epsilon_{ni} = 4 \cdot 10^{-2}$ to be consistent with Vinum et al. [14]. It should be stressed that the factor $\mathcal{P}_T \cdot \epsilon_{ni} \cdot (T_{extr} - T_0)$ that comes into play in the modeling of non-ideality overestimates the difference between the ideal and the real situation, as it leads to adding a fraction ϵ_{ni} of the absorption rate that would be reached at T_O in the fictitious case where $\mathcal{P}(T)$ would be linear between T_0 and T_{extr}. Hence, the real behavior is an intermediate between the prediction of the ideal model and that of the non-ideal model, as shown on figure 4. None of the models takes into account the range of temperatures below $T_{extr} - 200\ K$: this low temperature zone is not of interest in the present work.

2.2. Conventional vs. induction reactors

Based on the above-described model, simulations are performed to predict the behavior of the reactors described hereafter. Each part of the study is driven in the ideal case, then in the non-ideal case to assess the impact of non-ideality.

2.2.1. Parametric sensitivity

Four reactors, labeled 0 to 3, are studied in this part. Reactor 0 is a conventional reactor that is used as a reference (properties reported in table 3). Three induction reactors (#1 to 3) are considered. The properties of reactors #1 to 3 are related to those of reactor 0 as depicted on figure 5. The value of $\mathcal{P}_T(n)$ is obtained after successive trials-and-errors so that the methane outflow rate of induction reactor $\#n$ is the same as that of reactor 0.

The aim is to assess the stabilizing effect of induction (reactor 1 vs. reactor 0), but also to examine how this effect is impacted by the extrapolation temperature (reactor 2 vs. reactor 1) and by the intensity of the overcooling (reactor 3 vs. reactor 1).

Each of these four reactors is subject to a sensitivity analysis. Table 4 reports the parameters whose influence on the methane outflow rate as well as the catalyst hotspot temperature is determined. The sensitivity of quantity ϕ (methane outflow rate or hotspot temperature) to parameter X is obtained as follows: a "perturbed" reactor is simulated, with all parameters equal to those of the unperturbed reactor, except for parameter X that takes the perturbed value X^{pert}.

These simulation results enable to calculate the absolute and normalized sensitivities according to equations 13 and 14 respectively [26]:

$s_{\phi\backslash X} = \frac{\phi^{pert} - \phi}{X^{pert} - X}$ (Eq. 13)

$S_{\phi\backslash X} = \frac{X}{\phi} \cdot s_{\phi\backslash X}$ (Eq. 14)

2.2.2. Stable region extension

For the second part of the study, four reactors are compared (labeled A to D). Reactor A is a conventional reactor, the other three reactors are induction reactors. Their properties are the same as reactor 0 of the previous part (table 3), except for the catalyst density ρ_{cat}^{mix} which takes the value 700 kg/m^3 (it was 160 kg/m^3 for reactor 0). The induction-related properties of reactors B to D are reported table 5. For each reactor, the coolant temperature is gradually increased in increments of 1 K until a runaway occurs between two successive steady states. The catalyst hotspot temperature and the methane yield are computed for each value of the coolant temperature. The goal is to

analyze how the stable region (in the sense of the absence of a runaway) can be extended with the help of induction. The effect of $\{T_{extr}, \mathcal{P}_T\}$ on this extension can be detected by the comparison of reactors B to D.

3. Results and discussion

3.1. General observations (ideal $\mathcal{P}(T)$ dependence)

The quantities of interest are reported in table 6 for reactor 0. After the simulation results of reactor 0, the induction parameters of reactors #1 to 3 are determined. These parameters are reported in table 7. The comparison of reactor #2 to reactor #1 shows that the higher the value of T_{extr}, the lower the required value of $\mathcal{P}_T$. It can be understood as follows: for a given T_{cool} and a desired temperature of the reaction medium, $\mathcal{P}$ needs to be the same whatever T_{extr}. Hence, a low value of $\mathcal{P}_T$ has to be chosen when T_{extr} is high so that $\mathcal{P}$ remains unchanged according to equation 11. This reasoning is of course qualitative only. The actual behavior of a reactor is more complex, because the temperature of the catalyst is not equal to that of the inert medium, and spatial effects play an important role.

Comparing reactor 3 to reactor 1 confirms that a stronger overcooling implies a higher inductive heat supplement, to keep the energy balanced.

The outputs of reactors #1 to 3 are reported table 7. The hotspot temperature of the induction reactors is lower than that of reactor 0, even though the difference is small. The temperature profiles in reactors #1 to 3 are more homogeneous than in reactor 0 in the axial direction (figure 6). In the radial direction, the temperature gradients are higher when the coolant temperature is lower. This remark implies that a colder coolant leads to achieving the conversion in a more uniform manner in the axial direction, but not in the radial direction. The modification of $\{T_{extr}; \mathcal{P}_T\}$ does not seem to have a significant influence on the uniformity of the temperature profile (reactor 1 vs. reactor 2).

Figure 7 shows the temperature difference ($T_{cat} - T_{inert}$) profile. The catalyst is hotter than the inert medium in most of the reaction volume, even for induction reactors. In other words, the induction-

heated inert pellets do not necessarily heat the catalytic pellets. Rather, the induction makes the inert pellets just hot enough so as to limit the heat transfer from a catalytic pellet to its immediate vicinity (inert pellets and macroscopic gas). That transfer would otherwise be higher (overcooling).

3.2. Parametric sensitivity analysis (ideal $\mathcal{P}(T)$ dependence)

Table 8 reports the simulation results of reactors #0 to 3, when the perturbations are done based on table 4. The sensitivities calculated according to equations 13 and 14 are shown on figures 8 and 9. The stability enhancement due to the induction (in comparison to reactor 0) is more or less significant, depending on the perturbed parameter and on the considered output. More specifically:

- the stabilization of the hotspot temperature is stronger than that of the methane outflow rate;
- a perturbation of the coolant temperature is moderated more efficiently than a perturbation of the catalyst activity or inlet gas composition.

These two observations can be explained by the fact that the induction term is present in the energy balance only: the chemical stabilization comes as a side-effect of the temperature stabilization. Comparing the three induction reactors to each other, it can be seen that parameters $\{T_{extr}; \mathcal{P}_T; T_{cool}\}$ do have an impact on the parametric sensitivity. As the theory goes, the stabilizing effect of induction can be quantified by the negative value of $\frac{\partial \dot{Q}_{induc}}{\partial T}$ (part 1.2). This quantity cannot be accessed directly, because the various thermal power terms of equation 3 are related to the catalytic phase (where the reaction actually occurs [27, 28]) while the inductive power is associated to the inert phase. Strictly speaking, $\dot{Q}_{induc}$ should therefore measure how the induction on inert pellets affects the thermal power transferred between the catalytic pellets and their vicinity. However, this quantity will be assumed to be approximately proportional to $\mathcal{P}(T_{inert})$:

$\frac{\partial \dot{Q}_{induc}}{\partial T} \propto \frac{\partial \mathcal{P}}{\partial T_{inert}}$, which is more negative when $\mathcal{P}_T$ is higher (equation 15).

$\frac{\partial \mathcal{P}}{\partial T_{inert}} = -\mathcal{P}_T$ if $T_{inert} < T_{extr}$ (Eq. 15)

The simulation results appear to be completely coherent with these theoretical considerations:

i) For a given value of T_{cool}, a low T_{extr} is favorable to stabilization (reactor 1 vs. reactor 2). It was underlined earlier that the lower the value of T_{extr}, the higher the value of $\mathcal{P}_T$, so the stabilization is enhanced (equation 15). A safety margin has to be kept though, because the stabilizing effect totally disappears if T_{inert} exceeds T_{extr}. In the end, T_{extr} should be as close as reasonably possible, but not lower, than the allowed hotspot temperature of the inert medium.

ii) For a given value of T_{extr}, a low T_{cool} is favorable to stabilization (reactor 3 vs. reactor 1). In this case, the high $\mathcal{P}_T$ associated to the intense overcooling implies the very negative value of $\frac{\partial \mathcal{P}}{\partial T_{inert}}$.

3.3. Stable region extension (ideal $\mathcal{P}(T)$ dependence)

The steady-state hotspot temperature and methane yield of reactors A to D are reported figure 10. Induction reactors allow to access a hotspot temperature of 650 to 660 K and a methane yield in the 45-50% range before a runaway is triggered. Reactor A can't exceed a 30% yield, as it undergoes a runaway (extreme parametric sensitivity).

The comparison of reactor B to reactor D suggests that a higher $\mathcal{P}_T$ is associated to a lower pre-runaway value of T_{cool}. This remark is coherent with the theory: for a given reaction medium temperature, a high $\mathcal{P}_T$ implies that $\mathcal{P}$ is high as well, so the coolant temperature has to be low enough to provide a sufficient overcooling (equation 11). A similar reasoning explains why a high T_{extr} is associated to a low pre-runaway T_{cool} (reactor B vs. reactor C).

In terms of efficiency, reactor D allows a slightly higher methane yield than reactor B. The explanation is the same as that given in part 3.2, concerning the stabilizing effect of a high $\mathcal{P}_T$ (equation 15). Interestingly, reactor C remains stable up to a higher yield than reactors B and D, despite the fact that $-\mathcal{P}_T$ is less negative for reactor C. It turns out that the hotspot temperature of the inert medium reaches 654 K for reactor C: reactors B and D don't remain stable under such conditions, since they can't benefit from the stabilizing effect of induction above 653 K. This tends to confirm the fact that the proper choice of T_{extr} is crucial to guarantee the highest stability.

3.4. Effect of the non-ideality

The aim of this part is to examine how the deviation between the ideal and the non-ideal $\mathcal{P}(T)$ dependence impacts the results and conclusions obtained so far. The characteristics of reactors #1 to 3 and the corresponding simulation results, for the non-ideal case, are respectively reported in tables 9 and 10. It can be seen that the required $\mathcal{P}_T$ that results in the desired methane outflow rate are a little bit lower in the non-ideal case, compared to the ideal case. This is simply due to the fact that the non-ideal case gives a value of $\mathcal{P}$ that becomes significantly higher than that of the ideal case when one approaches the extrapolation temperature. Figures 11 and 12 show that the stability improvement in the non-ideal case is qualitatively the same as that obtained in the ideal case. However, it appears that the sensitivities are slightly closer to each other in the non-ideal case. This observation can be checked more specifically by calculating $s_{\phi\backslash X}(non-ideal)/s_{\phi\backslash X}(ideal)$ (resp. $S_{\phi\backslash X}(non-ideal)/S_{\phi\backslash X}(ideal)$), as reported on figure 13 (resp. 14). The reactor that is the less impacted by the non-ideality is reactor #2. Indeed, since T_{extr} is higher for reactor #2, the hotspot temperature of the reactor is further from T_{extr} in the case of reactor #2 compared to the other reactors. Therefore only a small difference does exist between the ideal and the non-ideal slopes at the hotspot temperature. On the opposite, reactor #3 is the most impacted by non-ideality. This can be explained by the fact that reactor #3 is the reactor whose $\mathcal{P}_T$ is the most strongly affected by the non-ideality.

The effect of non-ideality can also be examined through the stable zone extension (figure 15). Here again, the stability enhancement is qualitatively unchanged by the non-ideality. For all three reactors (B to D), the pre-runaway yield is lower than that of the ideal case. This is due to the fact that $\partial\mathcal{P}/\partial T_{inert}$ tends to become less negative prematurely in the non-ideal case, compared to the ideal case where $\partial\mathcal{P}/\partial T_{inert}$ remains constantly negative (as long as it doesn't cancel). Interestingly, even with a gradual cancelation of $\partial\mathcal{P}/\partial T_{inert}$ (no threshold effect), reactor C remains the most stable. $\partial\mathcal{P}/\partial T_{inert}$ is not exactly equal to zero for reactors B and D at the hotspot temperature of reactor C, nevertheless $\partial\mathcal{P}/\partial T_{inert}$ is more negative for reactor C at this temperature.

The observations made in this part have to be viewed with caution. The non-ideality had the same properties in all the cases (same shape of $\mathcal{P}\ (T)$, same ϵ_{ni}) : the nanoparticles were supposed to differ in extrapolation temperature only. In practice, nanoparticles that differ in extrapolation temperature might differ in other parameters. It remains interesting however to be aware that, from a theoretical point of view, the non-ideality per se only seems to slightly mitigate the conclusions obtained with an idealized model. In particular, whether or not there is a strict threshold where $\partial\mathcal{P}/\partial T$ goes from a constant negative value to zero, it's important to ensure that the characteristic temperature (extrapolation or Curie) always remains higher than the hotspot temperature with a sufficient margin.

3.5. Energy considerations

The specific absorption rate profiles of reactors #1 to 3 (ideal case) are shown figure 16. The subsequent inductive power of each reactor is calculated according to equation 16, it is reported in table 11.

$$\dot{Q}_{induc} = \int_{L_{reac}} \int_{r=0}^{R_{reac}} 2 \cdot \pi \cdot r \cdot \rho_{inert}^{mix}(r) \cdot \mathcal{P}(r,z) \cdot dr \cdot dz \quad \text{(Eq. 16)}$$

These values have to be compared to the power released by the reaction itself. The complete conversion of 1 m^3(STP)/h of a stoichiometric mixture (CO_2/H_2 = 20/80) into methane would release roughly 409 W, based on the reaction enthalpies indicated in part 1.2. The methane outflow rate of reactors #1 to 3 corresponds to a 40% yield, which means that the reaction releases 164 W in each reactor. It appears that the power consumption of the induction is very significant. Even though this power is collected as heat in the coolant, its exergetic value is way lower than that of the original electric power. Of course, this drawback has to be nuanced. The induction reactors that were studied here are definitely far from being optimal, since their characteristics were chosen in order to examine the physical effects of induction. The fact that the inlet gas is relatively cold also participates to the high inductive power consumption: the most upstream 4 cm of the reactor (5% of the reaction length) account for up to 15% of $\dot{Q}_{induc}$. A sufficient non-inducted inert length at the inlet would let

the gas pre-heat at no cost in terms of inductive power. Nevertheless, it is likely that the stabilization by a constant magnetic field amplitude would still involve a significant power consumption. This is a direct consequence of the founding principle of using induction together with overcooling: for the induction to be a strong stabilizer, it has to represent a part of the energy balance that is high enough so its variations make a real difference in the variations of the reaction medium temperature.

4. Conclusion and prospects

The aim of the present study was to prospect the theoretical benefit of induction as regards the stabilization of a reactor completing a highly exothermic reaction. Constant-in-time magnetic field conditions were chosen, in order to focus on the effect of the intrinsic negative feedback due to the thermal response of the induction-sensitive pellets. It was shown that this feedback enables a strong decrease in the parametric sensitivity of a reactor, and makes it possible to extend the stable operation into regions where a runaway would otherwise occur. The higher the magnetic induction, the better the stability enhancement of the reactor. The composition and size of the induction-sensitive nanoparticle have to be chosen carefully, so the decrease in absorption rate versus temperature remains high enough over a sufficient temperature range.

Compared to conventional rectors, the induction-based stabilization implies a higher level of complexity and requires extra energy consumption. The current readiness level of this technology is low, which means that many scientific and technical issues have to be addressed before the question of the cost-effectiveness be examined. First, the inductive power could be supplied to specific portions of the reaction length where the instabilities are the most prominent. Secondly, the control of the magnetic field as a function of the reaction yield is likely to greatly improve both the operation stabilization and the rational use of the inductive power, compared to the constant field conditions used in the present study. Such a regulation is expected to be particularly interesting if very dynamic operation is desired. In such situations, the characteristic time of the transitions might be shorter than the characteristic time of the adjustments that are compatible with conventional solutions. The control of the inductive field can be deemed instantaneous, which may eventually justify the investment effort related to the induction technology.

Acknowledgements: The authors would like to acknowledge the financial support provided by *Région Nouvelle Aquitaine*, France, for its financial support to this study.

Conflict of interest: The authors declare that they have no conflict of interest.

Appendix A.

The coefficients and thermophysical parameters used in the model are calculated as reported in table A.1. The balance equations of the tube wall and of the non-porous intake and outlet zones are reported table A.2. The fluxes in the equations of tables 1, 2 and A.2 are reported in table A.3.

Appendix B. Practical considerations

According to Cao et al. [46], the range of Curie temperatures that can be obtained with nanoparticles extends from ~300 K to ~1400 K. In other words, most exothermic reactions (including methanation) are usually performed at temperatures that are compatible with that of the accessible Curie temperatures. Although the extrapolation temperature used in the model is not equal to the Curie temperature, the difference is never expected to be very high, which means that the realistic extrapolation temperatures are also compatible with the usual reactions.

Another element to care about is the order of magnitude of the specific absorption rate $\mathcal{P}$. For example, Nemala et al. [19] obtained specific absorption rates in the order of a few dozen kW/kg (depending on the operation conditions - up to more than $9 \cdot 10^4$ W/kg) with Fe_3O_4 nanoparticles. Bordet et al. [18] even obtained specific absorption rates of $2 \cdot 10^6$ W/kg with iron carbide nanoparticles developed in a context of methanation. These values are relative to the mass of nanoparticles, while the present work considers the mass of inert pellets (containing nanoparticle) as a reference. The concentration of the nanoparticles in the inert pellets can be adjusted depending on the needs. Moreover, as mentioned in part 2.1.2., decreasing the inductive field amplitude/frequency or the pulses duration leads to a decrease in the absorption rate. Since all the

values of $\mathcal{P}$ that are encountered in the present study are at least 2 orders of magnitude lower than 90 kW/kg_{inert}, these values can be deemed realistic. The same reasoning can be driven for the parameter $\mathcal{P}_T$ used in the model: a moderation of the slope is synonymous with a decrease of $\mathcal{P}$. Nemala et al. obtained a slope in the order of a few hundred W/kg/K (up to more than 800 W/kg/K). The values of $\mathcal{P}_T$ that are used in the present work are typically 2 orders of magnitude lower than 800 W/kg_{inert}/K, making them realistic.

References

1. Villermaux J. Réacteurs chimiques – Principes. Techniques de l'ingénieur J4010 (1994).

2. Van Welsenaere R J., Froment G F. Parametric sensitivity and runaway in fixed bed catalytic reactors. Chemical Engineering Science 25 (1970). p. 1503-1516.

3. Shouman A R. A review of one aspect of the thermal-explosion theory. Journal of Engineering Mathematics 56-2 (2006). p. 179-184.

4. Morbidelli M., Varma A. Parametric sensitivity and runaway in fixed-bed catalytic reactors. Chemical Engineering Science 41:4 (1986). p. 1063-1071. DOI: 10.1016/0009-2509(86)87193-7

5. Fache A., Marias F., Guerre V., Palmade S. Optimization of fixed-bed methanation reactors: Safe and efficient operation under transient and steady-state conditions. Chemical Engineering Science 192 (2018). p. 1124-1137. DOI: 10.1016/j.ces.2018.08.044

6. Rönsch S., Schneider J., Matthischke S., Schlüter M., Götz M., Lefebvre J. Prabhakaran P., Bajohr S. Review on methanation – From fundamentals to current projects. Fuel 166 (2016). p. 276-296. DOI: 10.1016/j.fuel.2015.10.111

7. Guilera J., Andreu T., Basset N., Boeltken T., Timm F., Mallol I., Morante J R. Synthetic natural gas production from biogas in a waste water treatment plant. Renewable Energy 146 (2020). p. 1301-1308. DOI: 10.1016/j.renene.2019.07.044

8. Ducamp J. Conception et optimisation d'un réacteur-échangeur structuré pour l'hydrogénation du dioxyde de carbone en méthane de synthèse dédié à la filière de stockage d'énergie électrique renouvelable. Doctoral thesis, university of Strasbourg (2015).

9. Hwang S., Linke P., Smith R. Heterogeneous catalytic reactor design with optimum temperature profile II: application of non-uniform catalyst. Chemical Engineering Science 59:20 (2004). p. 4245-4260. DOI: 10.1016/j.ces.2004.05.036

10. Bremer J., Sundmacher K. Operation range extension via hot-spot control for catalytic CO2 methanation reactors. Reaction Chemistry & Engineering 6 (2019). DOI: 10.1039/C9RE00147F

11. Eigenberger G., Schuler H. Reactor stability and safe reaction engineering. Chemie Ingenieur Technik 58:8 (1986). p. 655-665

12. Idakiev V. V., Lazarova P. V., Bück A., Tsotsas E., Mörl L. Inductive heating of fluidized beds: Drying of particulate solids. Powder Technology 306 (2017). p. 26-33. DOI: 10.1016/j.powtec.2016.11.011

13. Idakiev V. V., Bück A., Mörl L., Tsotsas E. Inductive heating of fluidized beds: mobile versus stationary heat exchange elements. Drying Technology 37 (2019). p. 652-663. DOI: 10.1080/07373937.2018.1526190

14. Vinum M.G., Almind M.R., Engbaek J.S., Vendelbo S.B., Hansen M.F., Frandsen C., Bendix J., Mortensen P.M. Dual function Cobalt-Nickel nanoparticles tailored for high-temperature induction-heated steam methane reforming. Angewandte Chemie 57:33 (2018). p. 10569-10573. DOI: 10.1002/ange.201804832

15. Zhao X. Curie temperature measurement of ferromagnetic nanoparticles by using calorimetry. M.Sc. thesis of Wright State University (2014).

16. Hwang J H., Nagai T., Ohji T., Sando M., Toriyama M., Niihara K. Curie temperature anomaly in lead zirconate titanate/silver composites. Journal of the American Ceramic Society 81:3 (2005). DOI: 10.1111/j.1151-2916.1998.tb02394.x

17. Lopez-Dominguez V., Hernàndez J M., Tejada J., Ziolo R F. Colossal reduction in Curie temperature due to finite-size effects in CoFe2O4 nanoparticles. Chemistry of Materials 25 (2013). DOI: 10.1021/cm301927z

18. Bordet A., Lacroix L-M., Fazzini P-F., Carrey J., Soulantica K., Chaudret B. Magnetically Induced Continuous CO2 Hydrogenation Using Composite Iron Carbide Nanoparticles of Exceptionally High Heating Power. Angewandte Chemie International Edition 55:51 (2016). DOI: 10.1002/anie.201609477

19. Nemala H., Thakur J.S., Naik V.M., Vaishnava P.P., Lawes G., Naik R. Investigation of magnetic properties of Fe3O4 nanoparticles using temperature dependent magnetic hyperthermia in ferrofluids. Journal of applied physics 116, 034309 (2014). DOI: 10.1063/1.4890456

20. Fache A., Marias F., Guerre V., Palmade S. Intermittent operation of fixed-bed methanation reactors: a simple relation between start-up time and idle state duration. Waste and Biomass Valorization (2018). p. 1-17. DOI: 10.1007/s12649-018-0507-3

21. Wulf C., Linssen J., Zapp P. Power-to-gas – Concepts, demonstration, and prospects. Hydrogen supply chain chapter 9 (2018). DOI: 10.1016/B978-0-12-811197-0.00009-9

22. Fache A., Marias F. Dynamic operation of fixed-bed methanation reactors: yield control by catalyst dilution profile and magnetic induction. Renewable Energy (2019). DOI: 10.1016/j.renene.2019.11.081

23. Xu J., Froment G. Methane Steam Reforming, Methanation and Water-Gas Shift: 1. Intrinsic Kinetics. AIChE journal 35:1 (1989). DOI: 10.1002/aic.69035010

24. Kerkhof P.J.A.M. A modified Maxwell-Stefan model for transport through inert membranes the binary friction model. Chemical Engineering Journal 64:3 (1990). p. 319-343.

25. Winterberg M., Tsotsas E. Modelling of heat transport in beds packed with spherical particles for various bed geometries and/or thermal boundary conditions. International Journal of Thermal Sciences 39:5 (2000). p. 556-570. DOI: 10.1016/S1290-0729(00)00251-9

26. Morbidelli M., Varma A. A generalized criterion for parametric sensitivity: application to thermal explosion theory. Chemical Engineering Science 43:1 (1988). p. 91-102.

27. Wijngaarden R.J., Kronberg A., Westerterp K.R. Industrial catalysis - optimizing catalysts and processes. Wiley-VCH (1998).

28. Balakotaiah V., Kodra D., Nguyen D. Runaway limits for homogeneous and catalytic reactors. Chemical Engineering Science 50:7 (1995). p. 1149-1171. DOI: 10.1016/0009-2509(94)00463-2

29. Winterberg M., Tsotsas E. A simple and coherent set of coefficients for modelling of heat and mass transport with and without chemical reaction in tubes filled with spheres. Chemical Engineering Science 55:5 (2000). p. 967-979. DOI: 10.1016/S0009-2509(99)00379-6

30. Giese M., Rottschäfer K., Vortmeyer D. Measured and modelled superficial flow profiles in packed beds with liquid flow. AIChE journal 44 (1998). p. 484-490. DOI: 10.1002/aic.690440225

31. Giese M. Strömung in porösen Medien unter Berücksichtigung effektiver Viskositäten. Dissertation, TU München (1998).

32. Fuller E.N., Schettler P.D., Giddins J.C. A new method for prediction of binary gas-phase diffusion coefficients. Ind Eng Chem. 58:5 (1966). p. 18–27. DOI: 10.1021/ie50677a00

33. Kee R., Coltrin M., Glarborg P. Chemically Reacting Flow: Theory and Practice. New Jersey, USA: Wiley (2005).

34. Sutherland W. The viscosity of gases and molecular force. Philosophical Magazine 5:36 (1893). p. 507-531. DOI: 10.1080/14786449308620508

35. Wilke C.R. A viscosity equation for gas mixtures. The Journal of Chemical Physics 18 (1950). p. 517-550. DOI: 10.1063/1.1747673

36. Eucken A. Über das Wärmeleitvermögen, die spezifische Wärme und die innere Reibung der Gase. Physik Z 14:8 (1913). p. 324-332.

37. Perry R.H. et al. Chemical engineers'handbook. McGraw-Hill chemical engineering series, Fourth edition (1963).

38. Tsotsas E., Schlünder E. On axial dispersion in packed beds with fluid flow: über die axiale dispersion in durchströmten festbetten. Chem Eng Process: Process Intensif. 24:1 (1988). p. 15–31. DOI: 10.1016/0255-2701(88)87002-8

39. Gunn D.J., Pryce D..Dispersion in Packed Beds. Trans. Inst. Chem. Engrs., 47, T341 (1969).

40. Fahien R.W., Smith J.M. Mass transfer in packed beds. AIChE journal 1:1 (1955). DOI: 10.1002/aic.690010104

41. Dixon A., Cresswell D. Theoretical prediction of effective heat transfer parameters in packed beds. AIChE journal 25:4 (1979). p. 663-676. DOI: 10.1002/aic.690250413

42. Zehner P., Schlünder E.U. Wärmeleitfähigkeit von schüttungen bei mässigen temperaturen. Chemie-lngenieur Technik, 42,933 (1970). DOI: 10.1002/cite.330421408

43. Tsotsas E., Wärmeleitfähigkeit von Schüttschichten. VDI-Wärmeatlas.Springer,Berlin/Heidelberg (2006). p. 422–430.

44. Gnielinski V. Formula for Calculating the Heat and Mass Transfer In Through Flow of a Fixed Bed at Medium and Large Peclet. Process-Technology 12 (1978). p. 63-366.

45. Gnielinski V. Equations for the calculation of heat and mass transfer during flow through stationary spherical packings at moderate and high Peclet numbers. Int. Chem. Eng. 21 (1981). p. 378-383.

46. Cao L-f., Xie D., Guo M-x., Park H.S., Fujita T. Size and shape effects on Curie temperature of ferromagnetic nanoparticles. Transactions of Nonferrous Metals Society of China 17 (2007). p. 1451-1455.

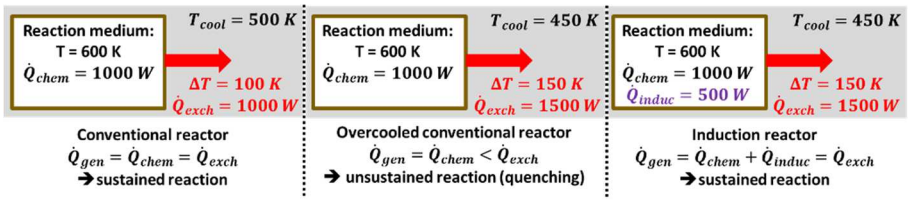

Figure 1. Progression from a conventional reactor to an induction reactor, via overcooling (arbitrary values are given for illustration purposes). The inductive power $\dot{Q}_{induc}$ is subject to an intrinsic negative feedback, and can also be quickly controlled via the magnetic field amplitude.

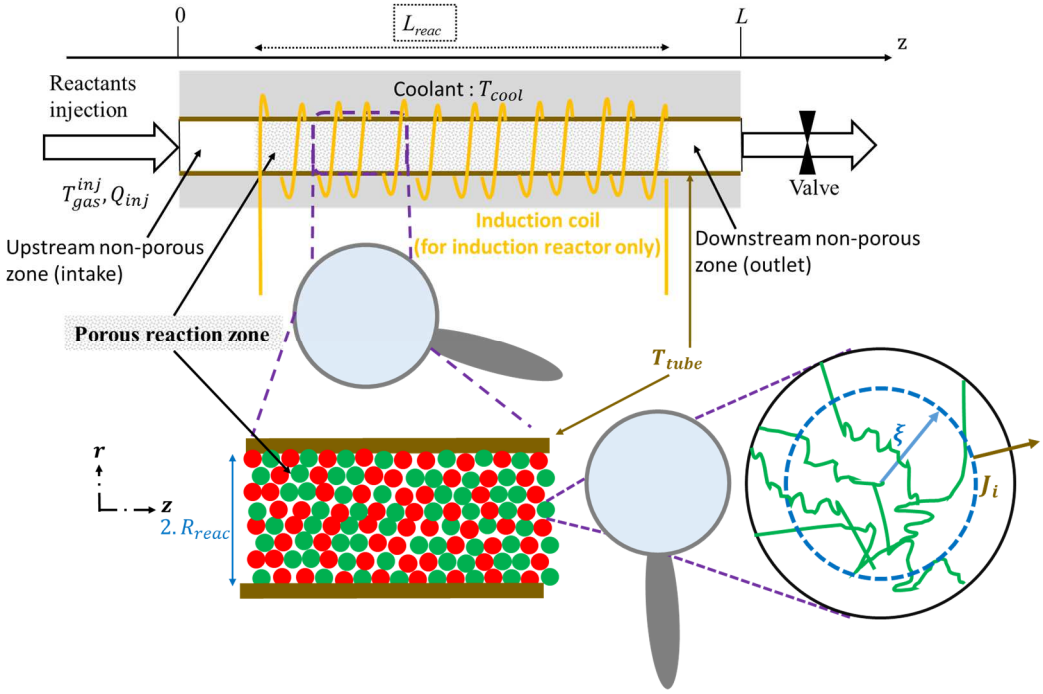

Figure 2. Architecture of the simulated reactor. The catalytic (green) pellets are mixed with inert (red) pellets. In the case of the induction reactor, the inert pellets are heated by the induction coil.

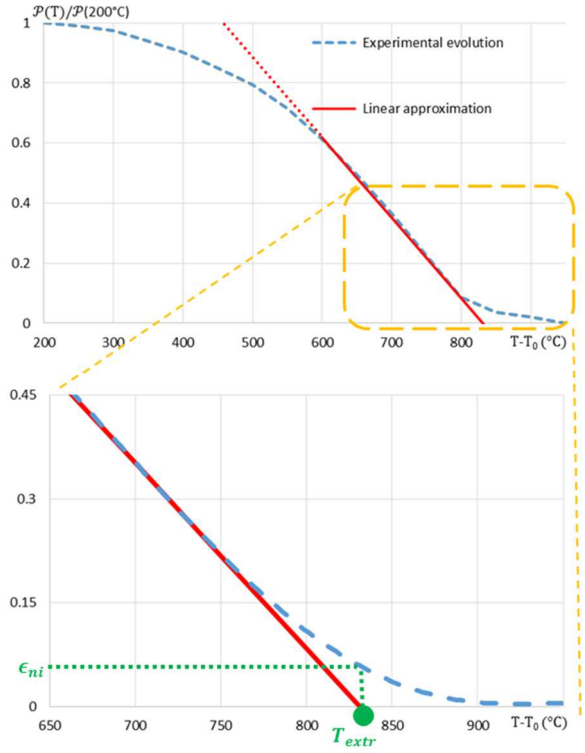

Figure 3. Local linearization and definition of the extrapolation temperature T_{extr} and of the non-ideality parameter ϵ_{ni}. The experimental curve is given for illustration purposes, based on the results of ref. 14 (Curie temperature: 892°C, magnetic field: 55 mT) after nondimensionalization.

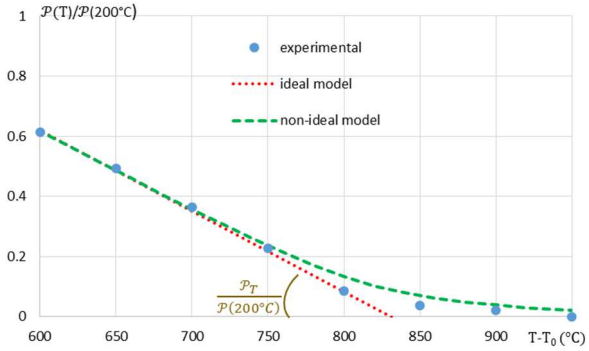

Figure 4. $\mathcal{P}$ as a function of the inert medium temperature, in the idealized case (Eq. 11) and in the non-ideal case (Eq. 12), for the nanoparticles studied by ref. 14 (Curie temperature: 892°C, magnetic field amplitude: 55 mT). All the reported quantities are divided by $\mathcal{P}(200°C)$ to keep the y-axis dimensionless.

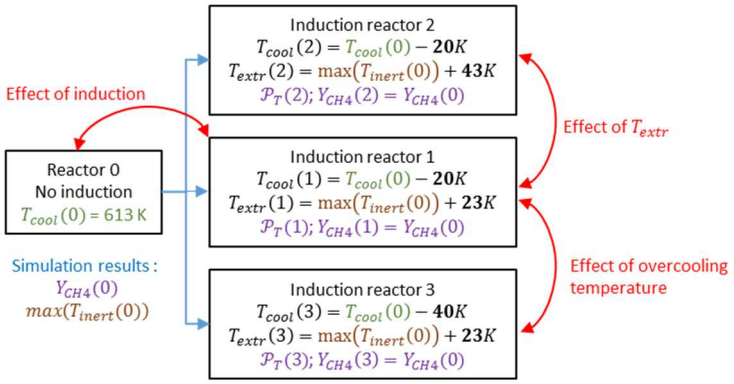

Figure 5. Properties differences between the reactors that are subject to the parametric sensibility analysis. All the other parameters (e.g. dimensions, catalyst density, etc) are identical to the parameters of reactor 0 (table 3).

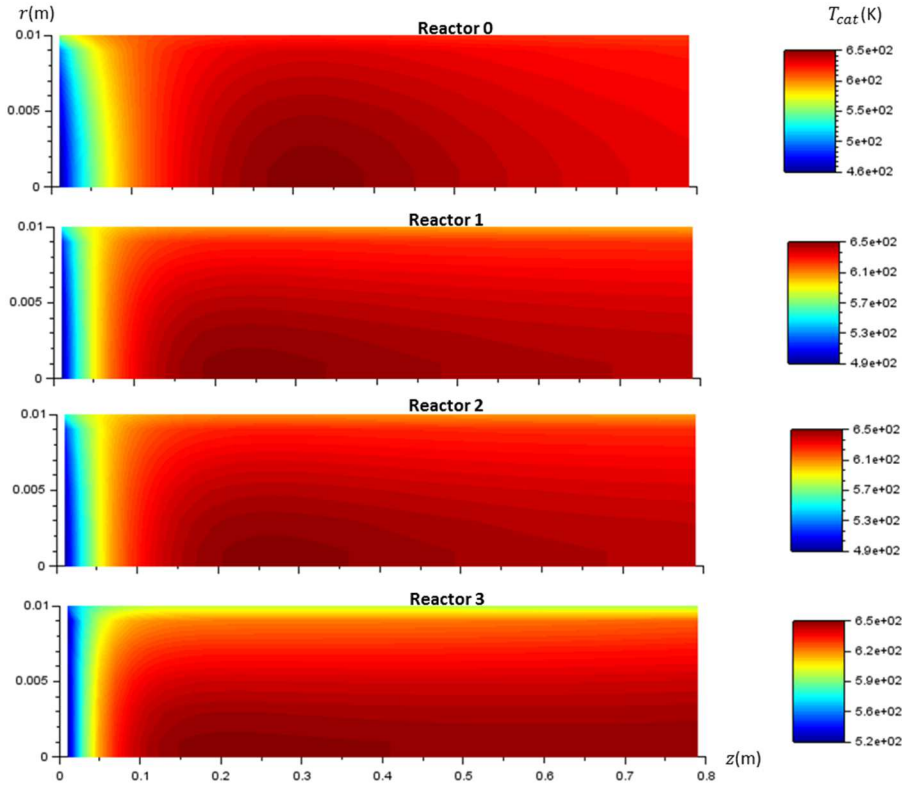

Figure 6. Temperature profile of the catalyst for reactors #0 to 3, in the idealized case.

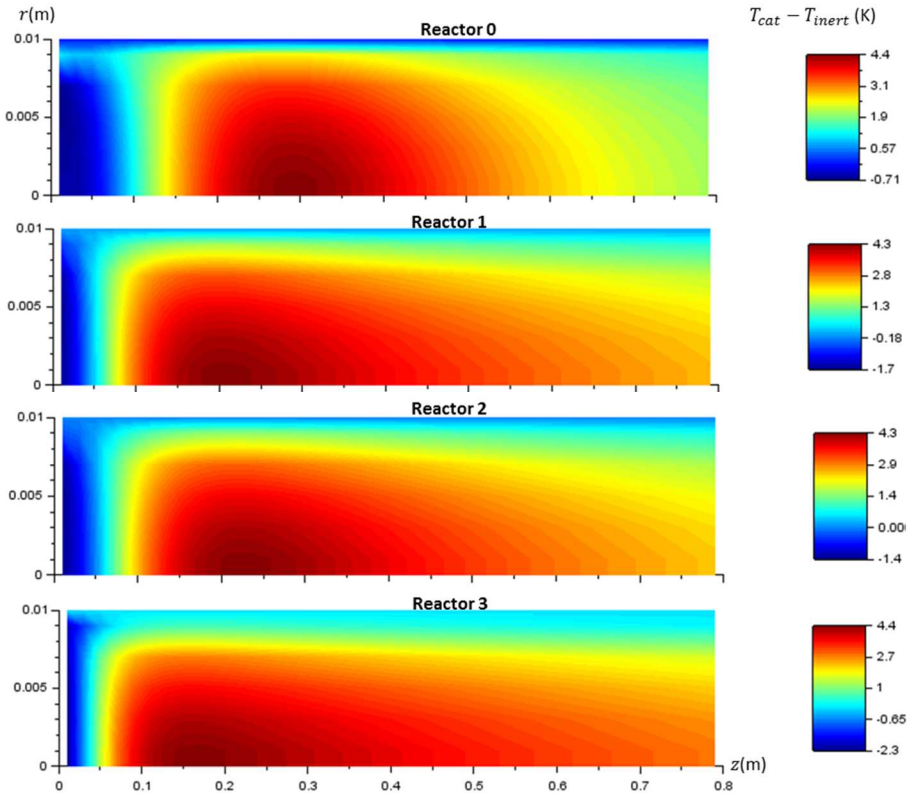

Figure 7. Difference in temperature profile (catalyst - inert) for reactors #0 to 3, in the idealized case.

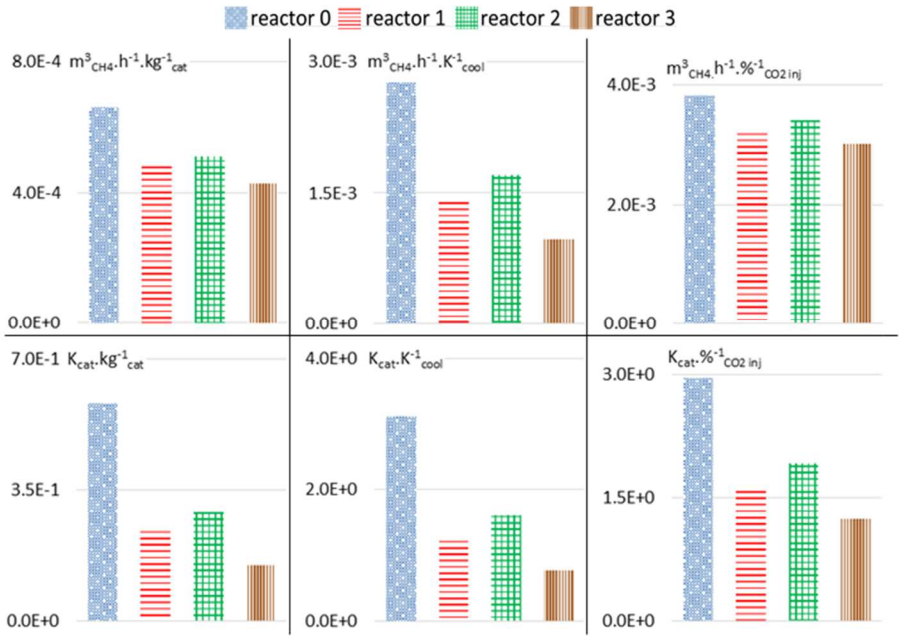

Figure 8. Absolute sensitivity of the methane outflow rate (top row) and of the catalyst hotspot temperature (bottom row) to the catalyst density (left column), to the coolant temperature (middle column) and to the CO_2 inflow fraction (right column). The $\mathcal{P}(T_{inert})$ relation is assumed to be ideal (Eq. 11).

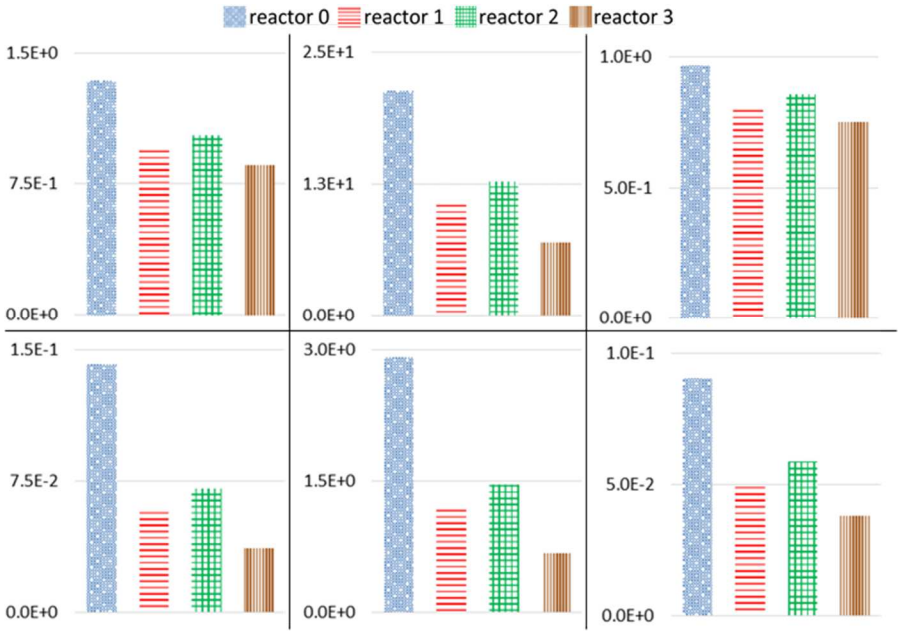

Figure 9. Normalized sensitivity of the methane outflow rate (top row) and of the catalyst hotspot temperature (bottom row) to the catalyst density (left column), to the coolant temperature (middle column) and to the CO_2 inflow fraction (right column). The $\mathcal{P}(T_{inert})$ relation is assumed to be ideal (Eq. 11).

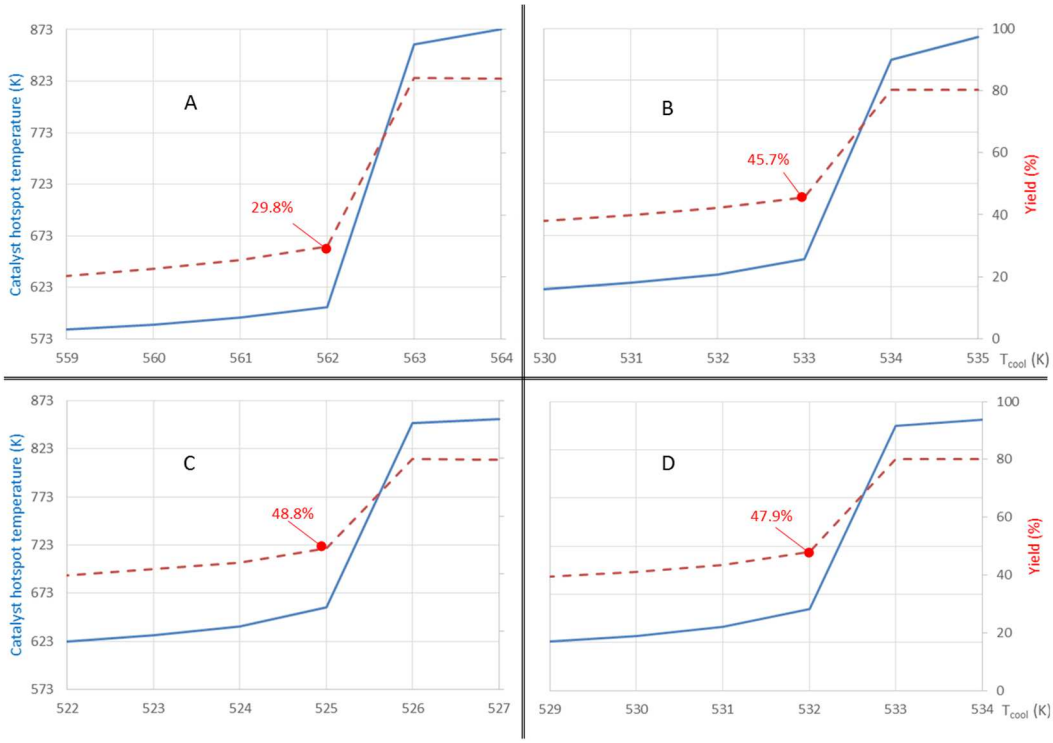

Figure 10. Steady-state catalyst hotspot temperature (continuous line) and methane yield (dashed line) as functions of the coolant temperature, for reactors A to D. The exact value of the pre-runaway yield is indicated in red. The $\mathcal{P}(T_{inert})$ relation is assumed to be ideal (Eq. 11).

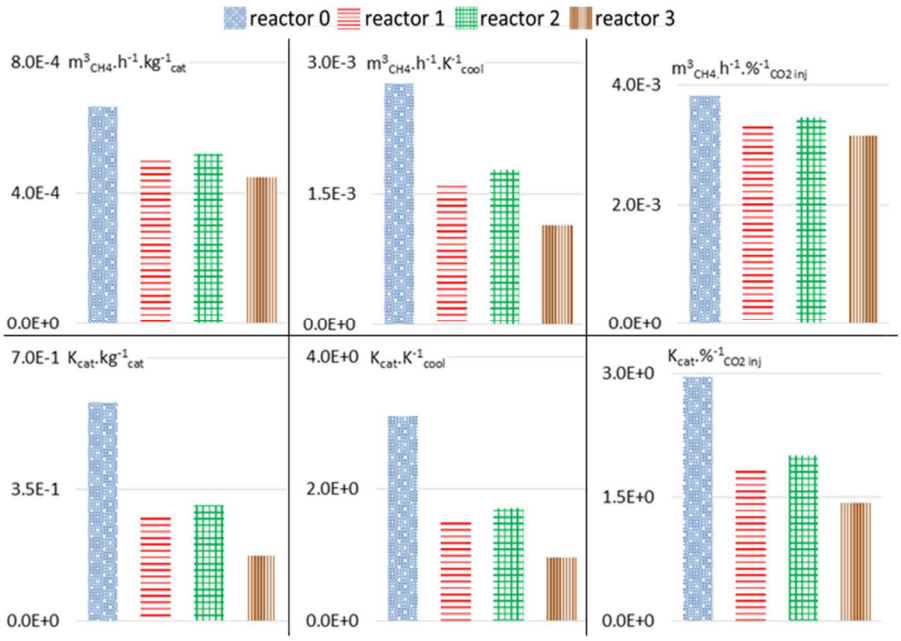

Figure 11. Absolute sensitivity of the methane outflow rate (top row) and of the catalyst hotspot temperature (bottom row) to the catalyst density (left column), to the coolant temperature (middle column) and to the CO_2 inflow fraction (right column). The $\mathcal{P}(T_{inert})$ relation is assumed to be non-ideal (Eq. 12).

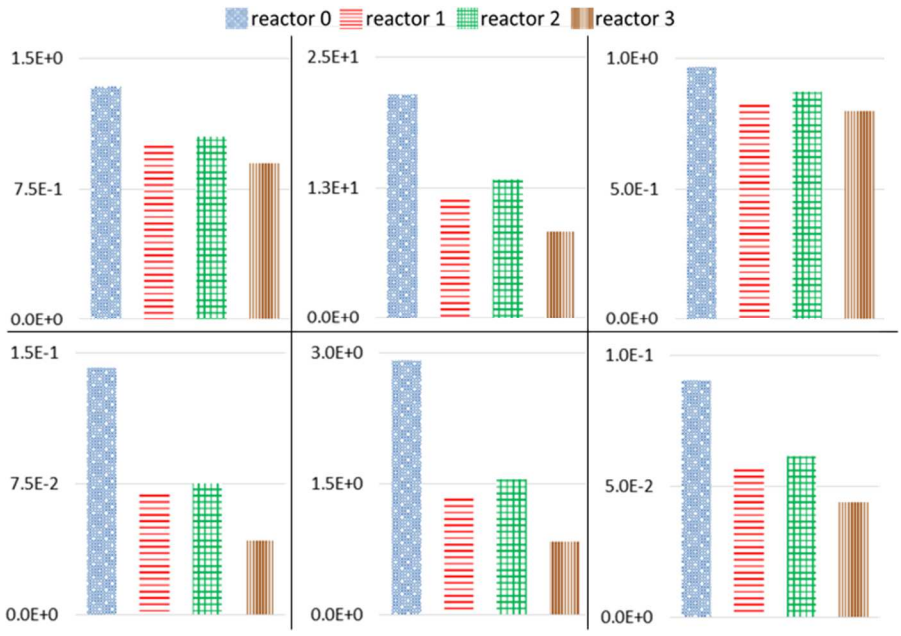

Figure 12. Normalized sensitivity of the methane outflow rate (top row) and of the catalyst hotspot temperature (bottom row) to the catalyst density (left column), to the coolant temperature (middle column) and to the CO_2 inflow fraction (right column). The $\mathcal{P}(T_{inert})$ relation is assumed to be non-ideal (Eq. 12).

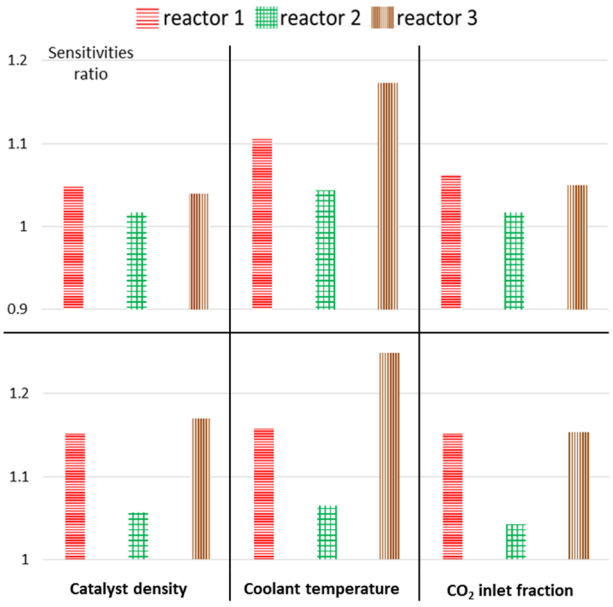

Figure 13. Absolute sensitivity with a non-ideal $\mathcal{P}(T_{inert})$ relation (Eq. 12), divided by the absolute sensitivity with an ideal $\mathcal{P}(T_{inert})$ relation (Eq. 11). Top row: methane outflow rate, bottom row: catalyst hotspot temperature.

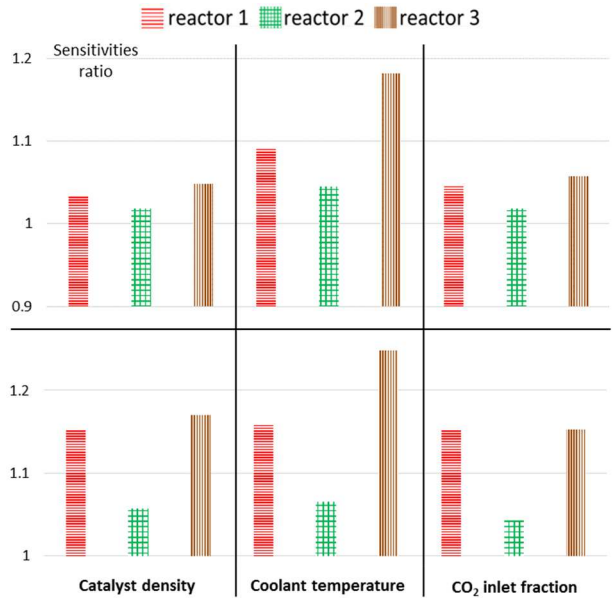

Figure 14. Normalized sensitivity with a non-ideal $\mathcal{P}(T_{inert})$ relation (Eq. 12), divided by the normalized sensitivity with an ideal $\mathcal{P}(T_{inert})$ relation (Eq. 11). Top row: methane outflow rate, bottom row: catalyst hotspot temperature.

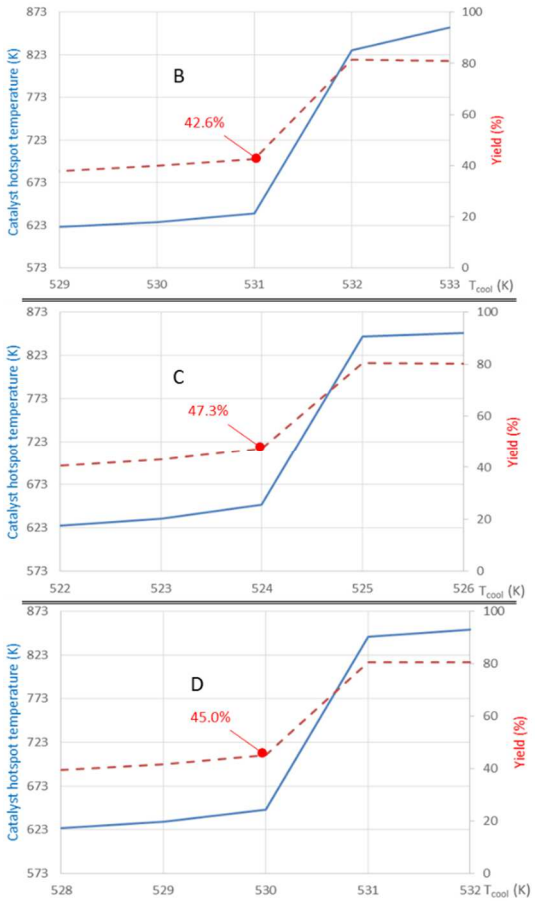

Figure 15. Steady-state catalyst hotspot temperature (continuous line) and methane yield (dashed line) as functions of the coolant temperature, for reactors B to D, when the $\mathcal{P}(T_{inert})$ relation is assumed to be non-ideal (Eq. 12). The exact value of the pre-runaway yield is indicated in red.

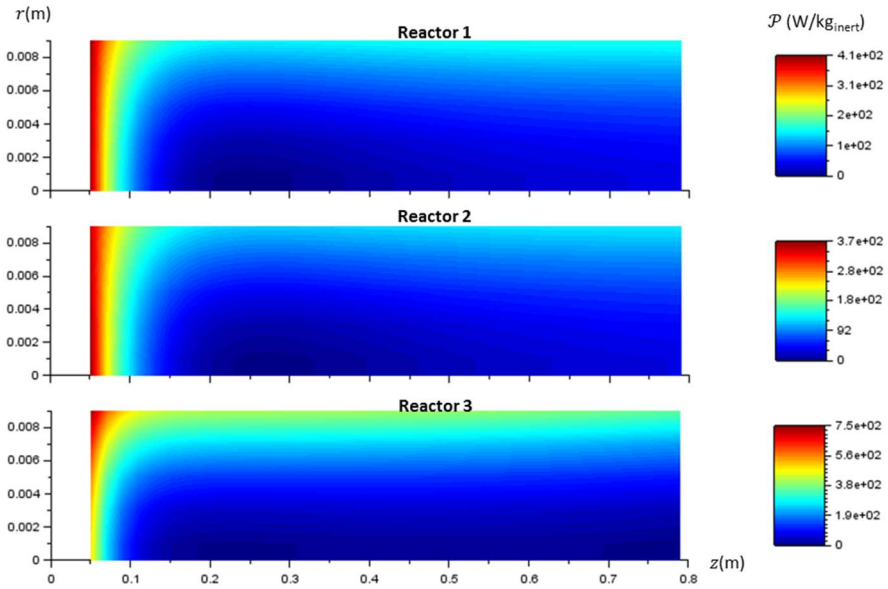

Figure 16. Specific absorption rate in reactors #1 to 3. The most upstream 5 cm (high $\mathcal{P}$ due to cold gas injection) are not shown, so that the gradients remain visible in the zone where the reaction actually occurs. The $\mathcal{P}(T_{inert})$ relation is assumed to be ideal (Eq. 11).

Microscopic	Macroscopic
Mass	
$\epsilon_{mic} \cdot \frac{\partial C_i}{\partial t} = \rho_{cat}^{mic} \cdot \dot{r}_i^m - \frac{1}{\xi^2}\frac{\partial \xi^2 \cdot J_i}{\partial \xi}$ (Eq. 4) reaction rate $\dot{r}_i^m$: Xu & Froment [23] B.C. : $R_i^v = a_{v_{cat}} \cdot \oiint_{\xi=d_p/2} J_i \cdot d^2S$	$\epsilon \cdot \frac{\partial C_i}{\partial t} = \frac{1}{r} \cdot \frac{\partial}{\partial r}\left(r \cdot D_{er,i} \cdot \frac{\partial C_i}{\partial r}\right) + R_i^v - \frac{\partial (C_i \cdot v_z)}{\partial z}$ (Eq. 5) B.C. : $C_i\left(z = \frac{L - L_{réac}}{2}, r\right) = C_i^{upstr}, \left(\frac{\partial C_i}{\partial r}\right)_{r=0} = 0, \left(\frac{\partial C_i}{\partial r}\right)_{r=R_{réac}} = 0$
Momentum	
$\left(\sum_{j\neq i} \frac{\chi_j}{D_{e,ij}} + D_{Kn,i} + \frac{B_0 \cdot P}{\mu_{i,mix}}\right) \cdot J_i = \sum_{j\neq i} \frac{\chi_i \cdot J_j}{D_{e,ij}} - \frac{1}{RT}\frac{\partial P_i}{\partial \xi}$ (Eq.6) [24] B.C. : continuity of P_i at the periphery pf the pellet ($\xi = d_p/2$)	$-\left(\frac{\partial P}{\partial z}\right) = 150 \cdot \frac{(1-\epsilon)^2}{\epsilon^3} \cdot \frac{\mu_{gas}}{d_p^2} \cdot v_z + 1.75 \cdot \frac{(1-\epsilon)}{\epsilon^3} \cdot \frac{\rho_{gas}}{d_p} \cdot {v_z}^2 + \frac{1}{r}\frac{\partial}{\partial r}\left(\mu_{eff} \cdot r \cdot \frac{\partial v_z}{\partial r}\right)$ (Eq. 7) [25] B.C. : $v_z(z, r = R_{réac}) = 0, P\left(z = \frac{L - L_{réac}}{2}, r\right) = P^{upstr}$
Energy	
Gas-catalytic solid equilibrium (see table 2)	$\epsilon \cdot \frac{\partial \left(\sum_i M_i \cdot C_i \cdot u_i(T_{gas})\right)}{\partial t} = a_{v_{cat}} \cdot \phi_{cat-g} + a_{v_{cat}} \cdot \sum_i h_i(T_{cat}) \cdot M_i \cdot J_i\left(\xi = \frac{d_p}{2}\right) + a_{v_{inert}} \cdot \phi_{inert-g}$ $+ \frac{1}{r} \cdot \frac{\partial}{\partial r}\left(r \cdot \lambda_{er}^{gaz} \cdot \frac{\partial T_{gas}}{\partial r}\right) + \sum_i \frac{1}{r} \cdot \frac{\partial}{\partial r}\left(r \cdot D_{er,i} \cdot \frac{\partial C_i}{\partial r}\right) \cdot M_i \cdot h_i(r) - \frac{\partial}{\partial z}\left(\sum_i M_i \cdot h_i \cdot C_i \cdot v_z\right)$ (Eq. 8) B.C. : $\left(\frac{\partial T_{gas}}{\partial r}\right)_{r=0} = 0, T_{gas}(r = R_{reac}) = T_{tube}, T_{gas}\left(z = \frac{L - L_{réac}}{2}, r\right) = T_{gas}^{upstr}$

Table 1. Balances in the gas phase. The balances of the upstream zone, the fluxes and the coefficients are detailed in appendix A.

Catalytic phase	Inert solid
$\epsilon_{mic} \cdot \frac{\rho_{cat}^{mix}}{\rho_{cat}^{mic}} \cdot \frac{24}{d_p^3} \cdot \int_{\xi=0}^{\frac{d_p}{2}} \xi^2 \cdot \frac{\partial\left(\sum_i M_i \cdot C_i^{mic} \cdot u_i(T_{cat})\right)}{\partial t} \cdot d\xi + \rho_{cat}^{mix} \cdot C_{cat} \cdot \frac{\partial T_{cat}}{\partial t} =$ $-a_{v_{cat}} \cdot \phi_{cat-g} - a_{v_{cat}} \cdot \sum_i h_i(T_{cat}) \cdot M_i \cdot J_i\left(\xi = \frac{d_p}{2}\right)$ $+f_{cat}^2 \cdot \frac{1}{r} \cdot \frac{\partial}{\partial r}\left(r \cdot \lambda^{cat-cat} \cdot \frac{\partial T_{cat}}{\partial r}\right) + 6 \cdot f_{cat} \cdot f_{inert} \cdot \frac{\lambda^{cat-inert}}{d_p^2} \cdot (T_{inert} - T_{cat})$ $+\frac{1}{2} \cdot f_{cat} \cdot f_{inert} \cdot \frac{1}{r} \cdot \frac{\partial}{\partial r}\left(r \cdot \lambda^{cat-inert} \cdot \left(\frac{\partial T_{cat}}{\partial r} + \frac{\partial T_{inert}}{\partial r}\right)\right)$ (Eq. 9) B.C. : $\left(\frac{\partial T_{cat}}{\partial r}\right)_{r=0} = 0, T_{cat}(r = R_{reac}, z) = T_{tube}(z)$	$\rho_{inert}^{mix} \cdot C_{inert} \cdot \frac{\partial T_{inert}}{\partial t} =$ $\rho_{inert}^{mix} \cdot \mathcal{P} - a_{v_{inert}} \cdot \phi_{inert-g}$ $+f_{inert}^2 \cdot \frac{1}{r} \cdot \frac{\partial}{\partial r}\left(r \cdot \lambda^{inert-inert} \cdot \frac{\partial T_{inert}}{\partial r}\right) + 6 \cdot f_{cat} \cdot f_{inert} \cdot \frac{\lambda^{cat-inert}}{d_p^2} \cdot (T_{cat} - T_{inert})$ $+\frac{1}{2} \cdot f_{cat} \cdot f_{inert} \cdot \frac{1}{r} \cdot \frac{\partial}{\partial r}\left(r \cdot \lambda^{cat-inert} \cdot \left(\frac{\partial T_{cat}}{\partial r} + \frac{\partial T_{inert}}{\partial r}\right)\right)$ (Eq. 10) B.C. : $\left(\frac{\partial T_{inert}}{\partial r}\right)_{r=0} = 0, T_{inert}(r = R_{reac}, z) = T_{tube}(z)$

Table 2. Energy balance in the solids of the reaction medium [22]. The fluxes and the coefficients are detailed in appendix A.

Parameter	Value	Parameter	Value
C_{cat}	$880\ \mathrm{J \cdot kg^{-1} \cdot K^{-1}}$	λ_{tube}	$1.1\ \mathrm{W \cdot m^{-1} \cdot K^{-1}}$
C_{inert}	$400\ \mathrm{J \cdot kg^{-1} \cdot K^{-1}}$	P_{out}	$4.5 \cdot 10^5$ Pa
d_p	$2 \cdot 10^{-3}$ m	R_{reac}	$1 \cdot 10^{-2}$ m
ϵ^{∞}	0.4	R_{tube}	$1.2 \cdot 10^{-2}$ m
ϵ_{mic}	0.6	r_{pore}	1.10^{-8} m
h_{c-t}	$400\ \mathrm{W \cdot m^{-2} \cdot K^{-1}}$	ρ_{cat}^{mic}	$2350\ \mathrm{kg \cdot m^{-3}}$
K_{valve}	$2 \cdot 10^{-9}\ \mathrm{m^3 \cdot s^{-1} \cdot Pa^{-1}}$	ρ_{cat}^{mix}	$160\ \mathrm{kg \cdot m^{-3}}$
L	0.84 m	ρ_{inert}^{mic}	$6800\ \mathrm{kg \cdot m^{-3}}$
L_{reac}	0.8 m	$(\rho C)_{tube}$	$2 \cdot 10^6\ \mathrm{J \cdot m^{-3} \cdot K^{-1}}$
λ_{cat}	$0.8\ \mathrm{W \cdot m^{-1} \cdot K^{-1}}$	τ	4.0
λ_{inert}	$20\ \mathrm{W \cdot m^{-1} \cdot K^{-1}}$	T_{gas}^{inj}	400 K
Q_{inj}	$1\ \mathrm{m^3(STP).h^{-1}}$	$\mathrm{Q_{inj,CO2}/Q_{inj,H2}}$	0.2/0.8

Table 3. Characteristics of reactor 0.

Qualitative nature of the perturbation	**Parameter X**	**Perturbed parameter X^{pert}**
Catalytic activity or load	ρ_{cat}^{mix}	$\left(\rho_{cat}^{mix}\right)^{pert} = 1.05 \times \rho_{cat}^{mix}$
Temperature	T_{cool}	$(T_{cool})^{pert} = T_{cool} + 1$ K
Chemical composition	$\mathrm{Q_{inj,CO2}/Q_{inj,H2}}$	$\left(\mathrm{Q_{inj,CO2}/Q_{inj,H2}}\right)^{pert} = 0.19/0.81$

Table 4. Parameters whose influence is calculated during the sensitivity analysis.

Reactor	B	C	D
$\mathcal{P}_T$(W/(K.kg$_{inert}$))	7.89	7.52	8.28
T_{extr} (K)	653	672	653

Table 5. Induction-related properties of reactors B to D (stable region extension).

Quantity	**Value**
Q_{CH4}^{out}	$7.92 \cdot 10^{-2}$ m^3(STP)/h
$\max(T_{cat})$	654 K
$\max(T_{inert})$	650 K

Table 6. Simulation results of reactor 0.

Reactor	**1**	**2**	**3**
Parameters			
T_{cool} (K)	593	593	573
T_{extr} (K)	673	693	673
$\mathcal{P}_T$(W/(K.kg$_{inert}$))	5.0	3.33	10.0
Simulation results			
Q_{CH4}^{out} (m^3(STP)/h)	$7.96 \cdot 10^{-2}$	$7.94 \cdot 10^{-2}$	$8.00 \cdot 10^{-2}$
$\max(T_{cat})$ (K)	652	653	653

Table 7. Characteristics of induction reactors # 1 to 3, when the $\mathcal{P}(T_{inert})$ relation is assumed to be ideal (Eq. 11).

Perturbed parameter ↓	Q_{CH4}^{out} (m³(STP)/h)	$\max(T_{cat})$ (K)
Reactor 0		
ρ_{cat}^{mix} (+5%)	$8.45 \cdot 10^{-2}$	659
T_{cool} (+1K)	$8.20 \cdot 10^{-2}$	657
Inlet composition (0.19/0.81)	$7.54 \cdot 10^{-2}$	651
Reactor 1		
ρ_{cat}^{mix} (+5%)	$8.34 \cdot 10^{-2}$	654
T_{cool} (+1K)	$8.10 \cdot 10^{-2}$	653
Inlet composition (0.19/0.81)	$7.64 \cdot 10^{-2}$	650
Reactor 2		
ρ_{cat}^{mix} (+5%)	$8.35 \cdot 10^{-2}$	655
T_{cool} (+1K)	$8.11 \cdot 10^{-2}$	655
Inlet composition (0.19/0.81)	$7.60 \cdot 10^{-2}$	651
Reactor 3		
ρ_{cat}^{mix} (+5%)	$8.35 \cdot 10^{-2}$	654
T_{cool} (+1K)	$8.10 \cdot 10^{-2}$	654
Inlet composition (0.19/0.81)	$7.70 \cdot 10^{-2}$	652

Table 8. Methane outflow rate and catalyst hotspot temperature of perturbed reactors # 0 to 3, when the $\mathcal{P}(T_{inert})$ relation is assumed to be ideal (Eq. 11).

Reactor	1	2	3
Parameters			
T_{cool} (K)	593	593	573
T_{extr} (K)	673	693	673
$\mathcal{P}_T$(W/(K.kg$_{inert}$))	4.75	3.21	9.00
Simulation results			
Q_{CH4}^{out} (m³(STP)/h)	$8.08 \cdot 10^{-2}$	$7.93 \cdot 10^{-2}$	$7.94 \cdot 10^{-2}$
$\max(T_{cat})$ (K)	654	653	653

Table 9. Characteristics of induction reactors # 1 to 3, when the $\mathcal{P}(T_{inert})$ relation is assumed to be non-ideal (Eq. 12).

Perturbed parameter ↓	Q_{CH4}^{out} (m³(STP)/h)	$\max(T_{cat})$ (K)
Reactor 1		
ρ_{cat}^{mix} (+5%)	$8.48 \cdot 10^{-2}$	656
T_{cool} (+1K)	$8.24 \cdot 10^{-2}$	655
Inlet composition (0.19/0.81)	$7.74 \cdot 10^{-2}$	652
Reactor 2		
ρ_{cat}^{mix} (+5%)	$8.35 \cdot 10^{-2}$	656
T_{cool} (+1K)	$8.11 \cdot 10^{-2}$	655
Inlet composition (0.19/0.81)	$7.58 \cdot 10^{-2}$	651
Reactor 3		
ρ_{cat}^{mix} (+5%)	$8.30 \cdot 10^{-2}$	655
T_{cool} (+1K)	$8.06 \cdot 10^{-2}$	654
Inlet composition (0.19/0.81)	$7.63 \cdot 10^{-2}$	652

Table 10. Methane outflow rate and catalyst hotspot temperature of perturbed reactors # 1 to 3, when the $\mathcal{P}(T_{inert})$ relation is assumed to be non-ideal (Eq. 12).

Reactor	1	2	3
$\dot{Q}_{induc}$ (W)	207	199	401

Table 11. Inductive power provided to reactors #1 to 3, when the $\mathcal{P}(T_{inert})$ relation is assumed to be ideal (Eq. 11).

Quantity	Expression
Porous medium properties	
proportion of catalytic/inert pellets in the mixture	$f_{cat} = \frac{\rho_{cat}^{mix}}{\rho_{cat}} = \frac{\rho_{cat}^{mix}}{(1-\epsilon)\cdot\rho_{cat}^{mic}}$, $f_{inert} = \frac{\rho_{inert}^{mix}}{\rho_{inert}} = 1 - \frac{\rho_{cat}^{mix}}{(1-\epsilon)\cdot\rho_{cat}^{mic}}$ (Eq. A.1)
surface areas of the spheres per unit of macroscopic volume	$a_{v_{cat}} = \frac{6}{d_p}\cdot\frac{\rho_{cat}^{mix}}{(1-\epsilon).\rho_{cat}^{mic}}$, $a_{v_{inert}} = \frac{6}{d_p}\cdot\left(1 - \frac{\rho_{cat}^{mix}}{(1-\epsilon).\rho_{cat}^{mic}}\right)$ (Eq. A.2)
macroscopic void fraction profile in the radial direction	$\epsilon(r) = \epsilon^{\infty}\cdot\left(1 + 1.36\cdot\exp\left(-5\cdot\frac{R_{reac}-r}{d_p}\right)\right)$ (Eq. A.3) [29, 30, 31]
Thermophysical and diffusion properties	
molecular diffusion of species i in species j / in the mixture	$D_{m,\ ij} = \frac{3.2\cdot10^{-3}\cdot T^{1.75}\cdot\left(M_i^{-1}+M_j^{-1}\right)^{1/2}}{P\cdot(v_i^{1/3}+v_j^{1/3})^2}$, $D_{m,\ i} = \frac{C_{tot}-C_i}{\sum_{j\neq i} C_j/D_{ij}}$ (Eq. A.4) [32, 33]
viscosity of pure gas i, of species i in the gas mixture, of the gas mixture	$\mu_i = \frac{C_{1i}\cdot T^{\frac{3}{2}}}{T+C_{2i}}$, $\mu_{i,mix} = \frac{\mu_i}{\sum_j \chi_j\cdot\Phi_{ij}}$, $\mu_{gas} = \sum_i \chi_i\cdot\mu_{i,mix}$ (Eq. A.5) [34, 35] with $\Phi_{ij} = \left(8\times\left(1+\frac{M_i}{M_j}\right)\right)^{-1/2}\left[1+\left(\frac{\mu_i}{\mu_j}\right)^{\frac{1}{2}}\left(\frac{M_j}{M_i}\right)^{\frac{1}{4}}\right]^2$
effective viscosity	$\mu_{eff} = 2\cdot\mu_{gas}\cdot\exp(2.10^{-3}\cdot Re_0)$ with $Re_0 = \rho_{gas}\cdot v_z\cdot\frac{d_p}{\mu_{gas}}$ (Eq. A.6)
thermal conductivity of the mixture / of gas i	$\lambda_{gas} = \frac{\sum_i \chi_i\cdot\lambda_i\cdot M_i^{1/3}}{\sum_i \chi i\cdot M_i^{1/3}}$ with $\lambda_i = \frac{9-\frac{5}{\gamma}}{4}\cdot\mu_i\cdot C_{p_i}$, $\gamma = C_{p_i}/C_{v_i}$ (Eq. A.7) [36, 37]
permeability of the micropores	$B_0 = \frac{r_{pore}^2}{20}\cdot\frac{\epsilon_{mic}}{\left(1-\epsilon_{mic}\right)^2}$ with $D_{e,ij} = \frac{\epsilon_{mic}}{\tau}\cdot D_{m,ij}$ (Eq. A.8) [27]
Knudsen diffusion coefficient in the micropores	$D_{Kn,i} = \frac{2\cdot\epsilon_{mic}\cdot r_{pore}}{3\cdot\tau}\left(\frac{8\cdot R\cdot T}{\pi\cdot M_i}\right)^{1/2}$ (Eq. A.9) [27]
matter dispersion coefficient	$D_{er,i} = \left(1-\sqrt{1-\epsilon}\right)\cdot D_{m,i} + v_z\cdot d_p/8$ (Eq. A.10) [38]
effective radial conductivity	$\lambda_{er}^{gas} = \frac{2}{3}\epsilon\cdot\lambda_{gas} + \frac{\rho_{gas}\cdot C_{p_{gas}}\cdot v_z\cdot d_p}{10}$ (Eq. A.11) [39, 40]
effective thermal conductivity	$\lambda^{inert-inert}$, $\lambda^{cat-cat}$: Zehner & Schlünder [41-43] based on the conductivity of the inert (catalytic resp.) solid $\lambda^{cat-inert}$: Zehner & Schlünder based on the harmonic mean of the inert and catalytic solids conductivity.

Table A.1. Thermophysical parameters and coefficients used in the model.

Intake zone	**Mass:** $S_{reac} \cdot \frac{L-L_{reac}}{2} \cdot \frac{\partial C_i^{upstr}}{\partial t} = Q_{inj,i} - 2\pi \int_{r=0}^{r=R_{reac}} r \cdot C_i\left(r, z=\frac{L-L_{reac}}{2}\right) \cdot v_z\left(r, z=\frac{L-L_{reac}}{2}\right) \cdot dr$ B.C. : $Q_{inj,i}$ is imposed (Eq. A.12) **Energy:** $S_{reac} \cdot \frac{L-L_{reac}}{2} \cdot \frac{\partial \sum_i C_i^{upstr} \cdot u_i^{upstr}}{\partial t} = 2\pi \frac{L-L_{reac}}{2} \cdot \left(T_{tube}^{upstr} - T_{gas}^{upstr}\right) \cdot h_{in\ out} + \sum_i Q_{inj,i} \cdot h_i\left(T_{gas}^{inj}\right)$ $- \sum_i 2\pi \int_{r=0}^{r=R_{reac}} r \cdot C_i\left(r, z=\frac{L-L_{reac}}{2}\right) \cdot v_z\left(r, z=\frac{L-L_{reac}}{2}\right) \cdot h_i\left(r, z=\frac{L-L_{reac}}{2}\right) \cdot dr$ B.C. : T_{gas}^{inj} imposed (Eq. A.13)
Outlet zone	**Mass:** $S_{reac} \cdot \frac{L+L_{reac}}{2} \cdot \frac{\partial C_i^{dwstr}}{\partial t} = 2\pi \int_{r=0}^{r=R_{reac}} r \cdot C_i\left(r, z=\frac{L-L_{reac}}{2}\right) \cdot v_z\left(r, z=\frac{L+L_{reac}}{2}\right) \cdot dr - Q_i^{out}$ B.C. : $Q_i^{out} = C_i^{dwstr} \cdot K_{valve} \cdot (P^{dwstr} - P_{out})$ (Eq. A.14) **Energy:** $S_{reac} \cdot \frac{L+L_{reac}}{2} \cdot \frac{\partial \sum_i C_i^{dwstr} \cdot u_i^{dwstr}}{\partial t} = 2\pi \frac{L-L_{reac}}{2} \cdot \left(T_{tube}^{dwstr} - T_{gas}^{dwstr}\right) \cdot h_{in\ out} - \sum_i Q_i^{out} \cdot h_i^{dwstr}$ $+ \sum_i 2\pi \int_{r=0}^{r=R_{reac}} r \cdot C_i\left(r, z=\frac{L-L_{reac}}{2}\right) \cdot v_z\left(r, z=\frac{L+L_{reac}}{2}\right) \cdot h_i\left(r, z=\frac{L+L_{reac}}{2}\right) \cdot dr$ (Eq. A.15)
Tube wall	$(\rho C)_{tube} \frac{\partial T_{tube}}{\partial t} = \frac{2\pi(R_{tube} \cdot \phi_{c-t} - R_{reac} \cdot \phi_{t-gs})}{S_{tube}} + \lambda_{tube} \frac{\partial^2 T_{tube}}{\partial z^2}$ B.C. : adiabatic extremities (Eq. A.16)

Table A.2. Complementary balance equations.

Flux term	Expression
catalyst / inert solids → gas	$\phi_{cat-g} = h_{s-g} \cdot (T_{cat} - T_{gas})$, $\phi_{inert-g} = h_{s-g} \cdot (T_{inert} - T_{gas})$ (Eq. A.17) h_{s-g} : Gnielinski [44, 45]
coolant → tube wall	$\phi_{c-t} = h_{c-t} \cdot (T_{cool} - T_{tube})$, $h_{c-t} = 400\ \mathrm{W/K/m^2_{c-t}}$ (Eq. A.18)
tube wall → reaction medium (gas + solids)	$\phi_{t-gs} = \phi_{t-g} + \phi_{t-cat} + \phi_{t-inert}$ (Eq. A.19) [22] $\phi_{t-g} = -\left(\lambda_{er}^{gaz} \cdot \frac{\partial T_{gas}}{\partial r}\right)_{r=R_{reac}}$ (Eq. A.20) $\phi_{t-cat} = -\left[\left(\frac{\rho_{cat}^{mix}}{(1-\epsilon)\cdot\rho_{cat}^{mic}}\right)^2 \cdot \lambda^{cat-cat} \cdot \frac{\partial T_{cat}}{\partial r} + \frac{1}{2} \cdot \frac{\rho_{cat}^{mix}}{(1-\epsilon)\cdot\rho_{cat}^{mic}} \cdot \left(1 - \frac{\rho_{cat}^{mix}}{(1-\epsilon)\cdot\rho_{cat}^{mic}}\right) \cdot \lambda^{cat-inert} \cdot \left(\frac{\partial T_{cat}}{\partial r} + \frac{\partial T_{inert}}{\partial r}\right)\right]_{r=R_{reac}}$ (Eq. A.21) $\phi_{t-inert} = -\left[\left(1 - \frac{\rho_{cat}^{mix}}{(1-\epsilon)\cdot\rho_{cat}^{mic}}\right)^2 \cdot \lambda^{inert-inert} \cdot \frac{\partial T_{inert}}{\partial r} + \frac{1}{2} \cdot \frac{\rho_{cat}^{mix}}{(1-\epsilon)\cdot\rho_{cat}^{mic}} \cdot \left(1 - \frac{\rho_{cat}^{mix}}{(1-\epsilon)\cdot\rho_{cat}^{mic}}\right) \cdot \lambda^{cat-inert} \cdot \left(\frac{\partial T_{cat}}{\partial r} + \frac{\partial T_{inert}}{\partial r}\right)\right]_{r=R_{reac}}$ (Eq. A.22)

Table A.3. Fluxes used in the balances of tables 1, 2 and A.2.

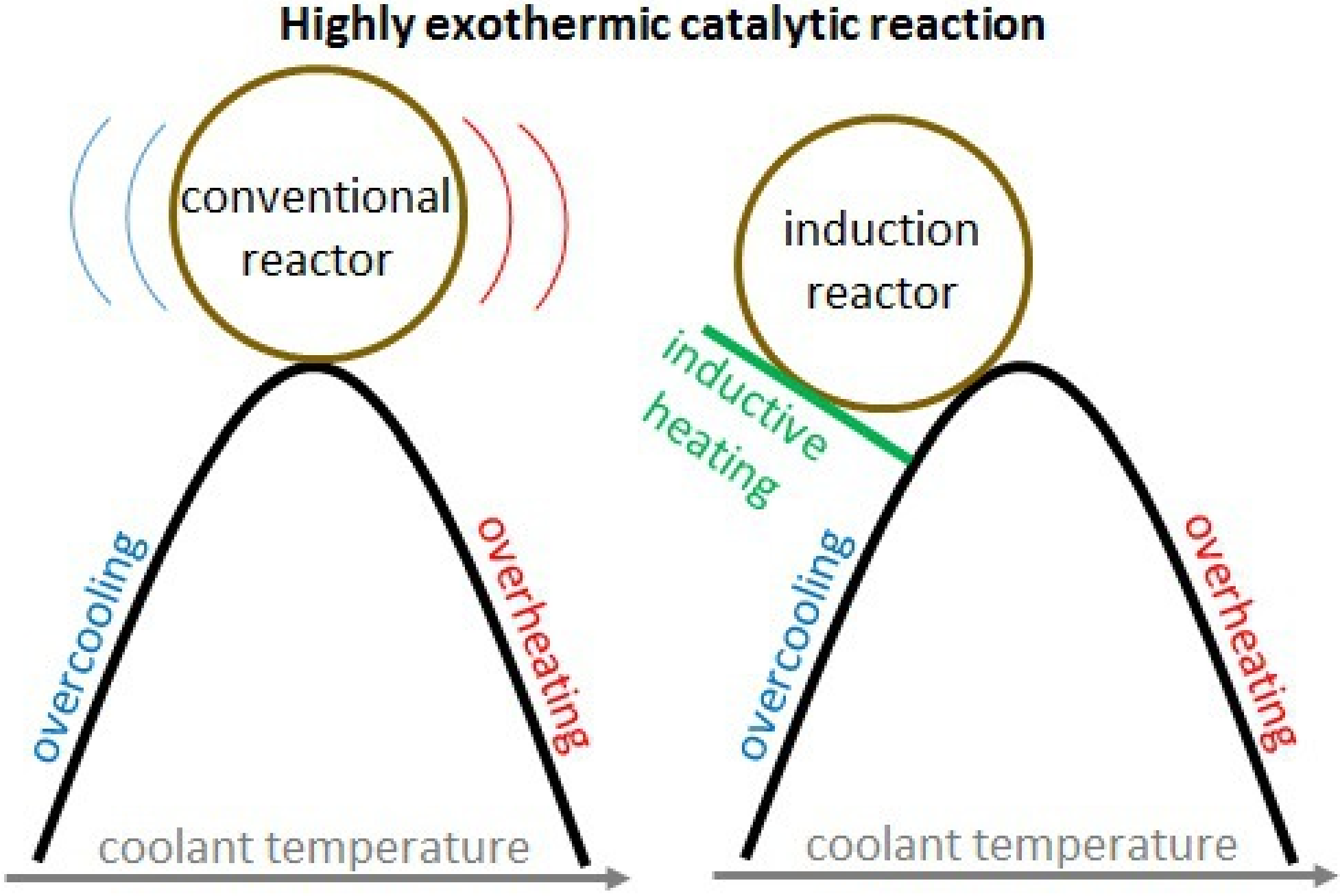
Highly exothermic catalytic reaction
conventional reactor
overcooling
overheating
coolant temperature
induction reactor
inductive heating
overcooling
overheating
coolant temperature